J. Fluid Mech. (2025), *vol.* 1016, A28, doi:10.1017/jfm.2025.10427

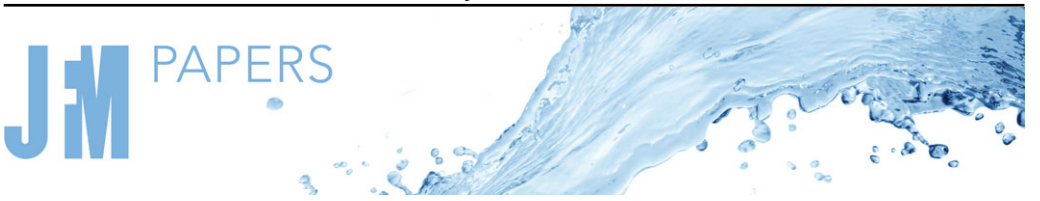

Scaling laws and space–time characteristics of wall pressure fluctuations in an axisymmetric boundary layer with varying pressure gradient

Guoqing Fan[1], **Hong Chen**[2], **Weiwen Zhao**[1] **and Decheng Wan**[1]

[1]Computational Marine Hydrodynamics Lab (CMHL), School of Ocean and Civil Engineering, Shanghai Jiao Tong University, Shanghai 200240, PR China

[2]Wuhan Second Ship Design and Research Institute, Wuhan 430205, PR China

Corresponding author: Weiwen Zhao, weiwen.zhao@sjtu.edu.cn

(Received 27 February 2025; revised 18 June 2025; accepted 30 June 2025)

Wall-resolved large-eddy simulations of flow over an axisymmetric body of revolution (DARPA SUBOFF bare model) at $Re_L = 1.1 \times 10^6$ are performed to investigate wall pressure fluctuations under the combined effects of transverse curvature and varying pressure gradients. Due to the coexistence of convex and concave streamwise curvatures, the flow in the stern region features alternating zones of favourable and adverse pressure gradients (APGs). The simulation validates experimental findings by Balantrapu *et al.* (2023, *J. Fluid Mech.,* vol. 960, A28), confirming that in APG-dominant axisymmetric boundary layers without streamwise curvatures, the root mean square wall pressure fluctuations ($p_{w,rms}$) decrease downstream alongside the wall shear stress (τ_w), maintaining a constant ratio $p_{w,rms}/\tau_w$. This study further finds that when streamwise curvatures and strong streamwise pressure gradient variations present, this relationship breaks down, suggesting that τ_w is not the dominant contributor to wall pressure fluctuations. Instead, the local maximum Reynolds shear stress $-\rho\langle u_s u_n\rangle_{max}$ emerges as a more robust pressure scaling parameter. Normalising the wall pressure spectra by $-\rho\langle u_s u_n\rangle_{max}$ yields better collapse across the entire stern region compared to conventional inner or mixed scaling methods. The magnitude and location of $-\rho\langle u_s u_n\rangle_{max}$ significantly influence the spectral levels of wall pressure fluctuations across different frequency bands. As the turbulence intensity and $-\rho\langle u_s u_n\rangle_{max}$ shift away from the wall, outer-layer structures – with larger spatial and temporal scales – dominate the coherence of wall pressure fluctuations. This mechanism drives sustained attenuation of high-frequency pressure fluctuations and a simultaneous increase in both the streamwise and transverse correlation lengths of wall pressure fluctuations over the stern region.

Key words: turbulence simulation, turbulent boundary layers

1. Introduction

As one of the unresolved challenges in fluid mechanics, the complexity of wall-bounded turbulence arises from its inherently chaotic and nonlinear nature. At high Reynolds numbers, the flow field around an axisymmetric body of revolution (BOR) is dominated by intricate near–wall turbulence. Wall pressure fluctuations, induced by velocity variations in the turbulent boundary layer (TBL), are regarded as the primary source of flow-induced noise. Comprehensive investigations into wall pressure fluctuations are crucial for understanding the underlying mechanisms of wall-bounded turbulence and for achieving accurate predictions of flow-induced noise in engineering applications.

For zero pressure gradient (ZPG) flow over flat plates, the spectral characteristics of wall pressure fluctuations and their scaling laws have been studied extensively, resulting in a wealth of experimental (Blake 1970; Schewe 1983; Farabee & Casarella 1991; Keith, Hurdis & Abraham 1992) and numerical (Kim 1989; Choi & Moin 1990; Panton, Lee & Moser 2017; Yang & Yang 2022) simulation data. In principle, the pressure fluctuations on the wall are typically determined by solving the Poisson equation

$$\frac{1}{\rho}\nabla^2 p = -2\frac{\partial u_i}{\partial x_j}\frac{\partial U_j}{\partial x_i} - \frac{\partial^2}{\partial x_i\,\partial x_j}(u_i u_j - \langle u_i u_j\rangle), \tag{1.1}$$

where p is the pressure fluctuation, ρ is the fluid density, and u_i and U_i $(i = 1, 2, 3)$ denote the velocity fluctuations and mean velocity, respectively. The terms on the right-hand side include the mean velocity gradient and the velocity fluctuations, which are referred to as the rapid and slow source terms, respectively. Given that the pressure Poisson equation is an elliptic partial differential equation, the fluctuating pressure on the wall typically results from the integrated effect of the velocity field within the TBL. Turbulence similarity theory (Farabee & Casarella 1991) suggests that wall pressure fluctuations across different frequency bands arise from contributions of various scales of physical quantities within the TBL. The low-frequency region is associated with large-scale motions in the outer layer, while the high-frequency region corresponds to small-scale motions in the inner layer, particularly in the logarithmic region. When normalised using the inner variables (wall friction velocity u_τ and viscous length $\delta_\nu = \nu/u_\tau$), the high-frequency wall pressure fluctuation spectra decay as ω^{-5}. Similarly, scaling with external variables (boundary layer thickness δ or displacement thickness δ^*, and outer edge velocity U_e) leads to spectral collapses in the low-frequency region. However, owing to the multi-scale nature of turbulence, no universal scaling law has been found that can collapse the pressure spectra across a wide frequency range and for different Reynolds numbers (Goody 2004; Rozenberg, Robert & Moreau 2012; Hu & Herr 2016; Lee 2018).

As a canonical BOR, the DARPA SUBOFF (Groves, Huang & Chang 1989) has been widely used for research purposes. Figure 1 shows the geometry of the bare hull (AFF1) configuration of the DARPA SUBOFF model. Over the past few decades, numerous researchers have conducted extensive experimental measurements (Huang *et al.* 1992; Jiménez *et al.* 2010*b*,*c*) and wall-resolved large-eddy simulations (WRLES) studies (Posa & Balaras 2016, 2020; Kumar & Mahesh 2018; Morse & Mahesh 2021, 2023; Liu *et al.* 2023) on this benchmark model at Reynolds numbers of the order of 10^6-10^7. These studies have focused primarily on hull forces, wake self-similarity, Reynolds number effects, and the influence of appendages. In comparison to ZPG flow over a flat plate, the investigation of wall pressure fluctuations on the SUBOFF model requires particular attention to two critical factors: convex transverse curvature and varying streamwise pressure gradient. The interaction between these factors gives rise to a more complex TBL

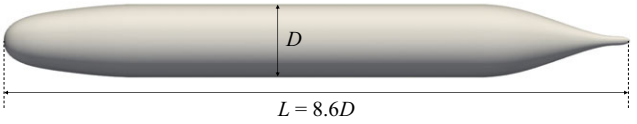

Figure 1. Geometry of the bare hull (AFF1) configuration of the DARPA SUBOFF model.

on the surface of the SUBOFF model. In many previous studies, these two aspects have often been analysed independently.

Convex transverse curvature is a critical factor that cannot be overlooked, especially when the ratio $\gamma = \delta/r$ of boundary layer thickness δ to the radius of curvature r is relatively large (Neves & Moin 1994). Compared to flat plates, axial flow over a cylinder exhibits a fuller velocity profile and higher surface friction coefficient C_f (Willmarth *et al.* 1976; Snarski & Lueptow 1995). Alam (2020) reports in his review that for $r^+ = ru_\tau/\nu < 2.5 \times 10^2$ (the superscript '+' denotes a non-dimensional parameter scaled by the wall friction velocity u_τ and the viscous length scale ν/u_τ), C_f increases exponentially, whereas for $r^+ > 2.5 \times 10^2$, the increase becomes relatively moderate. Regarding the influence of transverse curvature on wall pressure fluctuations, early experiments by Willmarth & Yang (1970) observed a slight increase of approximately 2 dB in the high-frequency range, offset by a reduction in low-frequency fluctuations. As a result, the root mean square (r.m.s.) of pressure fluctuations was comparable to that of a flat plate. Their study also noted a shorter correlation length scale for wall pressure fluctuations in both streamwise and transverse directions, suggesting that the generation of wall pressure fluctuations occurs closer to the wall than in the flat plate case. Neves, Parviz & Moser (1994) examined the effects of convex transverse curvature at $\gamma = 5$ ($r^+ \approx 43$) and $\gamma = 11$ ($r^+ \approx 21$). The results indicate that the Taylor frozen turbulence hypothesis (Taylor 1938) for wall pressure fluctuations remains valid, albeit with a lower convection velocity. As the curvature increases (and r decreases), the r.m.s. of pressure fluctuations decrease slightly. Interestingly, wall pressure fluctuations appear to be relatively insensitive when r^+ is large, particularly in cases involving high Reynolds numbers (Re_r, based on local radius of curvature r) and thin boundary layers (Piquet & Patel 1999). The mechanisms of near-wall turbulence production and self-sustaining processes are also closely analogous to those observed in flat plate flows.

The pressure gradient is another critical factor in flow over the DARPA SUBOFF model. Early experimental studies by Schloemer (1966) demonstrated that the convection velocity in adverse pressure gradient (APG) flows was lower than that in ZPG flows, and the coherence in the streamwise direction decayed more rapidly in APG compared to ZPG. The results also revealed that APG increased the low-frequency levels of wall pressure fluctuations without significantly affecting the high-frequency components. In contrast, favourable pressure gradients (FPGs) result in a stronger high-frequency content. However, due to the relatively large size of sensors used in early experiments, the measurements of high-frequency components were often inaccurate. Subsequent investigations (Cohen & Gloerfelt 2018) demonstrated that wall pressure fluctuations in APG flows exhibited faster attenuation in the mid-frequency range, and lower spectral levels in the high-frequency region. In addition to the inner peak, an outer peak – similar to that observed in high-Reynolds-number ZPG boundary layers (Monty *et al.* 2009; Marusic *et al.* 2010; Lee & Moser 2015) – was also identified in APG flows (Harun *et al.* 2013; Kitsios *et al.* 2017). An analysis of turbulence production (Kitsios *et al.* 2017) suggests that the combined effects of mean shear and large-scale motions contribute to the increased turbulence intensity in the outer layer, thereby amplifying the low-frequency spectral levels. As a consequence, some

studies (Simpson, Ghodbane & Mcgrath 1987; Na & Moin 1998; Abe 2017; Schatzman & Thomas 2017) have suggested that the maximum turbulent shear stress $\rho\langle|u'v'|\rangle_{max}$ can also be used as a scaling quantity for wall pressure fluctuations.

Research on wall pressure fluctuations in axisymmetric boundary layers, particularly when accounting for both convex transverse curvature and pressure gradient, remains relatively limited. Balantrapu *et al.* (2020) conducted an experimental investigation on an axisymmetric BOR with a small length-to-diameter ratio, providing wall pressure fluctuation spectra at discrete measurement locations on the stern. Compared to the SUBOFF model, the BOR used in their study featured an elongated stern with no curvature variation in the tail section along the streamwise direction, resulting in a stable APG. In subsequent studies, Balantrapu, Alexander & Devenport (2023) further revealed that as the flow decelerates downstream, the r.m.s. of wall pressure fluctuations decreases in tandem with the wall shear stress, both scaling consistently by approximately $7\tau_w$. Additionally, when scaled using mixed variables (τ_w as the pressure scale and U_e/δ as the frequency scale), the pressure fluctuations at all measurement locations collapsed within a range of 2 dB. In terms of numerical simulations, Zhou, Wang & Wang (2020) adopted a hybrid approach combining wall-modelled large-eddy simulations (WMLES) and WRLES (with WMLES for the nose and centre-body sections, and WRLES for the stern) to simulated the flow over the BOR under identical conditions, and compared the wall pressure fluctuation spectra at three discrete measurement points on the stern. The results showed good agreement with experimental data, indicating that WRLES can achieve accuracy comparable to experiments in predicting wall pressure fluctuations.

The aforementioned studies focus primarily on equilibrium TBLs, where the pressure gradient remains approximately constant, and the boundary layer inherently exhibits self-similarity. Only a few studies (Tanarro, Vinuesa & Schlatter 2020; Volino 2020; Caiazzo *et al.* 2023) have addressed the effects of streamwise curvature and the development of non-equilibrium boundary layers. In practice, engineering flows often involve curved surfaces, such as aerofoils and submarines, where the Clauser parameter (β_c) and acceleration parameter (K) exhibit strong variations along the streamwise direction. For instance, the stern of the SUBOFF model exhibits complex flow features, such as pressure gradients, transverse curvature, and combined convex and concave streamwise curvature. Morse & Mahesh (2021) investigated the evolution of the boundary layer along the hull under a streamline coordinate system. However, they did not pay extra attention to wall pressure fluctuations. To our knowledge, there are currently no publicly available experimental or high-fidelity WRLES data on wall pressure fluctuations for this benchmark model. While recent numerical studies (He *et al.* 2022; Zhou *et al.* 2022; Jiang, Liao & Xie 2024) have begun to address wall pressure fluctuations for the SUBOFF model, these efforts frequently suffer from two critical limitations: insufficient validation against experimental data, and inadequately resolved near-wall grids. The latter fail to meet the resolution requirements for accurately resolving wall pressure fluctuations at relevant Reynolds numbers. Additionally, these researches focus solely on the parallel mid-body region, while the evolution of wall pressure fluctuations at the stern of the SUBOFF model is more complex and has not yet been investigated. As a consequence, further investigation remains critically important to advance the fundamental understanding of wall pressure fluctuations and refine predictive models for turbulence and flow noise.

In the present study, WRLES of flow over the DARPA SUBOFF bare hull at $Re_L = 1.1 \times 10^6$ are performed within a finite volume framework. The selected Reynolds number is consistent with previous study of experiments (Jiménez *et al.* 2010*b*) and WRLES (Kumar & Mahesh 2018; Morse & Mahesh 2021, 2023). The primary objectives of this study are as follows: (i) to provide high-fidelity wall pressure fluctuation data for

flow over this benchmark model at $Re_L = 1.1 \times 10^6$; (ii) to investigate the evolution of wall pressure fluctuations under the combined effects of varying pressure gradients, transverse curvature, and streamwise curvature; (iii) to investigate the scaling laws of wall pressure fluctuations in the non-equilibrium axisymmetric boundary layer subjected to varying pressure gradient; (iv) to analyse the structures and space–time correlations of wall pressure fluctuations of the SUBOFF model; (v) to evaluate the applicability of existing flat-plate wall pressure fluctuation models to an axisymmetric BOR. The paper is organised as follows. In § 2, we provide details of the numerical methodology and the validation of the present WRLES. In § 3, we present the instantaneous flow field and boundary layer development around the SUBOFF model. The results of wall pressure fluctuations are analysed in § 4, with final conclusions drawn in § 5.

2. Numerical methodology and validation

2.1. *Governing equations*

Large-eddy simulations (LES) are incapable of resolving vortices of all scales in the flow field. By applying a filter to the incompressible Navier–Stokes equations, the governing equations for LES can be obtained as

$$\frac{\partial \tilde{u}_i}{\partial t} + \frac{\partial \tilde{u}_i \tilde{u}_j}{\partial x_j} = -\frac{1}{\rho}\frac{\partial \tilde{p}}{\partial x_i} + \nu \frac{\partial^2 \tilde{u}_i}{\partial x_j \partial x_j} - \frac{\partial \tau_{ij}^{sgs}}{\partial x_j}, \tag{2.1}$$

$$\frac{\partial \tilde{u}_i}{\partial x_i} = 0, \tag{2.2}$$

where $\tilde{u}_i$ ($i = 1, 2, 3$) is the filtered velocity component in the x_i direction, $\tilde{p}$ is the filtered pressure, ν is the kinematic viscosity of the fluid, and τ_{ij}^{sgs} is the subgrid-scale (SGS) stress term that is given by

$$\tau_{ij}^{sgs} = 2\nu_{sgs}\tilde{S}_{ij} + \tfrac{1}{3}\tau_{kk}^{sgs}\delta_{ij}, \tag{2.3}$$

with $\tilde{S}_{ij}$ the resolved strain rate tensor, δ_{ij} the Kronecker delta, and ν_{sgs} the SGS eddy viscosity. In this study, the wall-adapting local eddy viscosity (WALE) model (Nicoud & Ducros 1999) is applied to compute the eddy viscosity

$$\nu_{sgs} = (C_w \Delta)^2 \frac{\left(S_{ij}^d S_{ij}^d\right)^{3/2}}{\left(\tilde{S}_{ij}\tilde{S}_{ij}\right)^{5/2} + \left(S_{ij}^d S_{ij}^d\right)^{5/4}}, \tag{2.4}$$

where $C_w = 0.325$ is the WALE coefficient, Δ is the cube root of the local cell volume, and S_{ij}^d is the traceless symmetric part of the square of the velocity gradient tensor.

The present simulation is performed using the open-source CFD platform OpenFOAM. The spatial discretisation employs a second-order central differencing scheme for both convective and diffusive terms to ensure low numerical dissipation, which is critical for resolving turbulence structures in WRLES. The temporal term is discretised using a second-order implicit backward scheme. The PISO algorithm (Issa 1986) is employed to handle the pressure–velocity coupling, with three pressure corrections and one extra loop for non-orthogonality at each time step. The momentum equation is solved using the bi-conjugate gradient stabilised (PBiCGStab) solver with the diagonal-based incomplete LU (DILU) preconditioner. For the pressure Poisson equation, we use the conjugate gradient solver with the diagonal-based incomplete Cholesky preconditioner. The tolerance is set to 10^{-7}. The present numerical algorithm has been validated for a

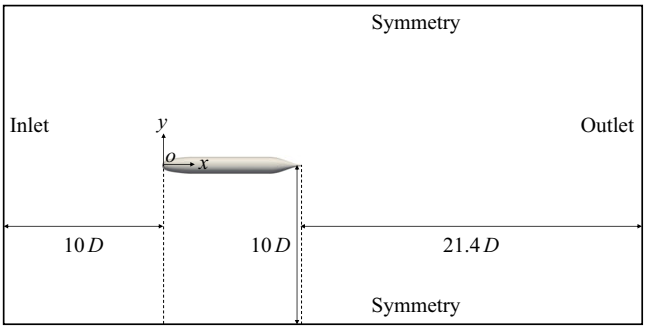

Figure 2. Computational domain.

variety of problems over a range of Reynolds numbers in our previous study (Fan *et al.* 2024*a*; He *et al.* 2024*b*; He, Zhao & Wan 2025), demonstrating good agreement with experimental and direct numerical simulations (DNS) data in terms of mean velocity profiles, Reynolds stresses and wall pressure statistics.

2.2. *Computational domain and mesh*

The computational domain and mesh are described as follows. Figure 2 shows the computational domain adopted in the present study, which is larger than domains used in Posa & Balaras (2016) and Kumar & Mahesh (2018). Taking the stagnation point at the bow of the hull as the origin, the x-axis is aligned with incoming flow direction. The computational domain extends over length $40D$, and width and height $20D$, where D represents the diameter at the parallel mid-body of the hull. The hull length is $L = 8.6D$, and the domain spans $-10D < x < 30D$, $-10D < y < 10D$ and $-10D < z < 10D$. An unstructured mesh is used in this study, with graded refinement applied near the hull. Our previous study (He *et al.* 2024*b*) on turbulent channel flow demonstrated that for WRLES, in addition to ensuring that the first wall-normal grid layer satisfies $\Delta y_w^+ < 1$, the spanwise (or azimuthal) grid resolution should also be kept below 15 to avoid log-law mismatch in the near-wall velocity profile. This constraint arises because near-wall velocity streaks, which contribute to wall friction, require relatively fine spanwise grid resolution. Furthermore, the streamwise grid resolution Δx^+ plays a crucial role in accurately capturing high-frequency wall pressure fluctuations, similar to the effect of sensor size on high-frequency measurements in experimental studies. As the streamwise grid is refined, the high-frequency content of the wall pressure spectrum increases and eventually converges to DNS results. In present study, given the primary focus on wall pressure fluctuations, the wake region is not further refined. The near-wall streamwise grid resolution at the mid-body is $\Delta x^+ = 24$, which is finer than resolutions used in previous studies (Kumar & Mahesh 2018; Morse & Mahesh 2021). The azimuthal grid resolution is $r^+\,\Delta\theta = 12$, and the height of the first grid layer is $\Delta y_w^+ = 0.92$. The total number of grids is approximately 540 million. The time step used in the simulation is $\Delta t^* = \Delta t\, U_\infty / L = 8.69 \times 10^{-5}$, ensuring that the Courant–Friedrichs–Lewy number is satisfied with $CFL < 1$. The unsteady simulations are run for six flow-past times, with the first 2.5 flow-past times used for flow development, and the remaining 3.5 flow-past times used for statistical analysis, which is longer than in the WRLES study by Kumar & Mahesh (2018) (two flow-past times for flow development, and two flow-past times used for data sampling). In Appendix A, we further examine the effect of the sampling time period to ensure that the flow is fully developed and the sampling duration is sufficient.

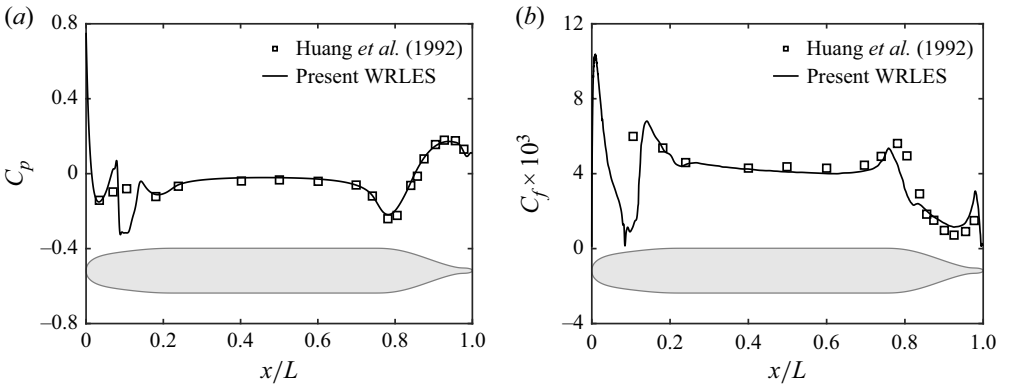

Figure 3. Mean pressure and skin friction coefficients on the hull. The experimental results (Huang *et al.* 1992) at $Re_L = 1.2 \times 10^7$ are shown for comparison.

To improve numerical stability and accelerate convergence in the WRLES, a steady-state Reynolds-averaged Navier–Stokes (RANS) simulation is first performed on the same computational mesh. The resulting steady-state pressure and velocity fields from the precursor RANS solution are then used as the initial conditions for the WRLES computation. For the boundary conditions, a uniform inflow is prescribed at the inlet to achieve a hull-length Reynolds number $Re_L = 1.1 \times 10^6$. At the outlet, a zero-gradient condition is imposed on the velocity field, while the pressure is set to zero. The SUBOFF model hull is assigned a no-slip velocity condition and a zero-gradient pressure condition. The remaining domain boundaries are treated as symmetry planes. At this Reynolds number, the flow remains predominantly laminar over a significant portion of the hull. To prompt rapid transition to turbulence, a numerical trip is introduced at the bow ($x/D = 0.75$) by applying a steady wall-normal velocity. The trip location is the same as that used in the experiments by Jiménez *et al.* (2010*b*) and the simulations by Kumar & Mahesh (2018) and Morse & Mahesh (2021). Following the perturbation, the flow quickly transitions from laminar to turbulent.

2.3. *Validation of present WRLES*

To validate the accuracy of the present numerical method, figure 3 shows the mean pressure and skin friction coefficient on the hull surface, which are defined as

$$C_p = \frac{p - p_\infty}{0.5\rho U_\infty^2}, \quad C_f = \frac{\tau_w}{0.5\rho U_\infty^2}, \tag{2.5}$$

where p_∞ represents the reference pressure, and τ_w denotes the wall shear stress. Since Jiménez's experiment (Jiménez *et al.* 2010*b*) for the DARPA SUBOFF model did not provide C_f data, and the reference pressure selection also differed from the experiment by Huang *et al.* (1992), the results here are only compared with Huang *et al.* (1992) at Reynolds number $Re_L = 1.2 \times 10^7$. The application of numerical tripping introduces minor fluctuations in the WRLES results within the bow region ($0.08 \leqslant x/L \leqslant 0.1$). The pressure coefficient C_p is known to be relatively insensitive to Reynolds number. However, the friction coefficient C_f is significantly affected by it, and the experimental C_f is scaled to the simulation Reynolds number using the scaling law $C_f \sim Re^{-0.2}$. This scaling is strictly valid only for TBLs under ZPG conditions. The predicted C_f in the parallel mid-body region shows good agreement with the scaled experimental data, but deviations

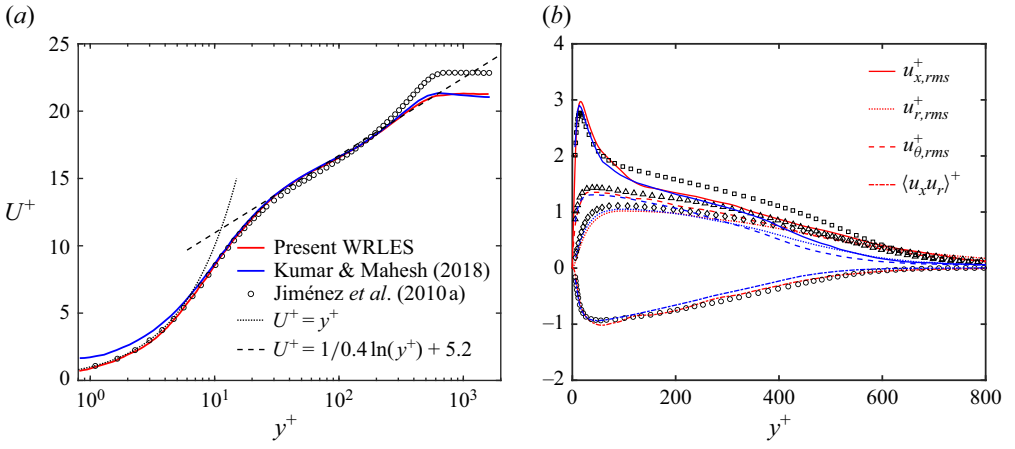

Figure 4. Mean flow characteristics of the TBL at the mid-body of the hull ($x/L = 0.42$): (*a*) mean streamwise velocity profile; (*b*) r.m.s. of velocity fluctuations ($u^+_{x,rms}$, $u^+_{r,rms}$, $u^+_{\theta,rms}$) and Reynolds stress $\langle u_x u_r \rangle^+$. The red line represents the present WRLES results, while the blue line corresponds to the WRLES results from Kumar & Mahesh (2018) at the same Re_L. The scatter points represent DNS results for a flat plate at $Re_\theta = 1551$ from Jiménez *et al.* (2010*a*).

appear in the stern region where strong APGs are present due to the limitations of the scaling law under non-equilibrium conditions.

Figure 4 presents the mean velocity profile, r.m.s. of velocity fluctuations ($u^+_{x,rms}$, $u^+_{r,rms}$, $u^+_{\theta,rms}$) and Reynolds stress $\langle u_x u_r \rangle^+$ profile at the mid-body ($x/L = 0.42$). The WRLES results (Kumar & Mahesh 2018) at the same Re_L, and DNS results (Jiménez *et al.* 2010*a*) for a flat plate at a momentum thickness Reynolds number $Re_\theta = 1551$, are shown for comparison. As mentioned in the Introduction, an axisymmetric TBL is characterised by slightly higher wall friction compared to a flat-plate TBL at similar Reynolds numbers. The outer edge velocity of the boundary layer is smaller, and this behaviour is consistent with observations reported in previous studies (Kumar & Mahesh 2018; Morse & Mahesh 2021). In terms of the r.m.s. of velocity fluctuations and Reynolds stress, the WRLES predictions for the near-wall inner layer agree well with both the WRLES results from Kumar & Mahesh (2018) and the DNS results for a flat plate from Jiménez *et al.* (2010*a*). The axisymmetric BOR exhibits a more rapid decay in wall-normal turbulence intensity compared to the flat plate. In the region where $y^+ > 100$, the r.m.s. values of streamwise velocity fluctuations are lower than the corresponding flat-plate results, which is also consistent with the findings of Kumar & Mahesh (2018).

Figure 5 shows the profiles of pressure coefficients (C_p), streamwise velocity (U_x), radial velocity (U_r) and r.m.s. of velocity fluctuations ($u_{x,rms}$, $u_{r,rms}$, $u_{\theta,rms}$) at the stern of the hull ($x/L = 0.904$ and 0.978). The WRLES results from Kumar & Mahesh (2018) at the same Re_L, and the experimental results from Huang *et al.* (1992) at $Re_L = 1.2 \times 10^7$, are shown for comparison. Here, r_0 is the local radius of the hull at the stern, and R is the radius of the mid-body. The velocity profiles in figures 5(*c*,*d*) reveal the progressive thickening of TBL in the stern region. Due to flow separation, the peaks of velocity fluctuation r.m.s. in figure 5(*f*) shift away from the wall. From figures 5(*e*,*f*), it can be observed that the predicted r.m.s. of velocity fluctuations within the boundary layer agree well with the data of Kumar & Mahesh (2018). However, the predicted results outside the boundary layer ($(r - r_0)/R > 0.75$) are slightly lower than those of Kumar & Mahesh (2018). Given that the present study focuses primarily on the flow dynamics within the boundary layer, we did not apply additional grid refinement in the wake region. While

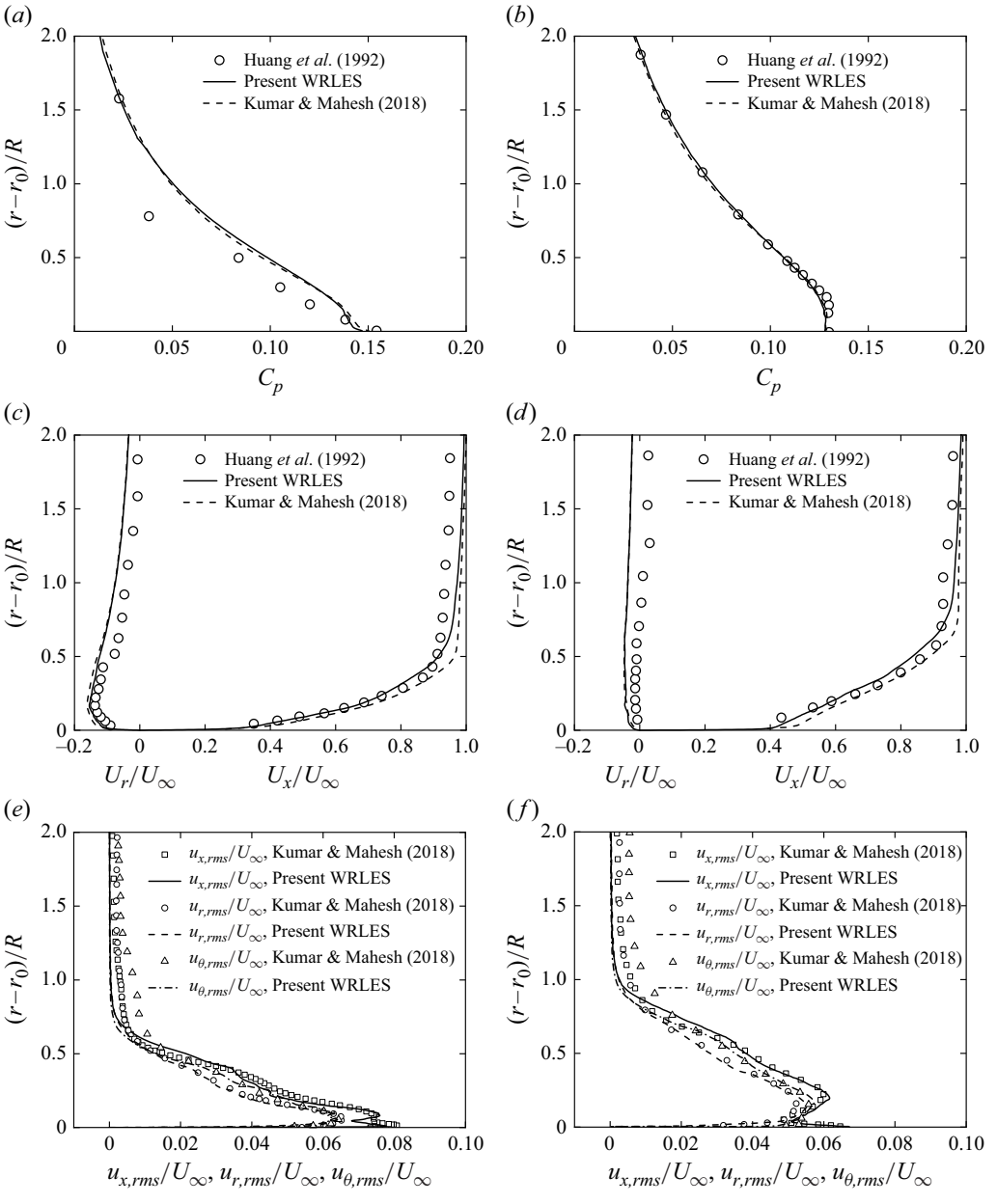

Figure 5. Mean flow characteristics of the TBL at the stern of the hull, for (*a*,*c*,*e*) $x/L = 0.904$, (*b*,*d*,*f*) $x/L = 0.978$. (*a*,*b*) Mean pressure coefficients profile; (*c*,*d*) mean streamwise (U_x) and radial (U_r) velocity profile; (*e*, *f*) r.m.s. of velocity fluctuations ($u_{x,rms}$, $u_{r,rms}$, $u_{\theta,rms}$). The WRLES results from Kumar & Mahesh (2018) at the same Re_L, and the experimental results from Huang *et al.* (1992) at $Re_L = 1.2 \times 10^7$, are shown for comparison.

the WRLES study by Kumar & Mahesh (2018) specially targeted the wake. The grid resolution at the stern away from the wall is lower than that in Kumar & Mahesh (2018), which can result in higher dissipation and lower predicted r.m.s. of velocity fluctuations. Overall, the WRLES predictions in this study agree well with existing WRLES datasets

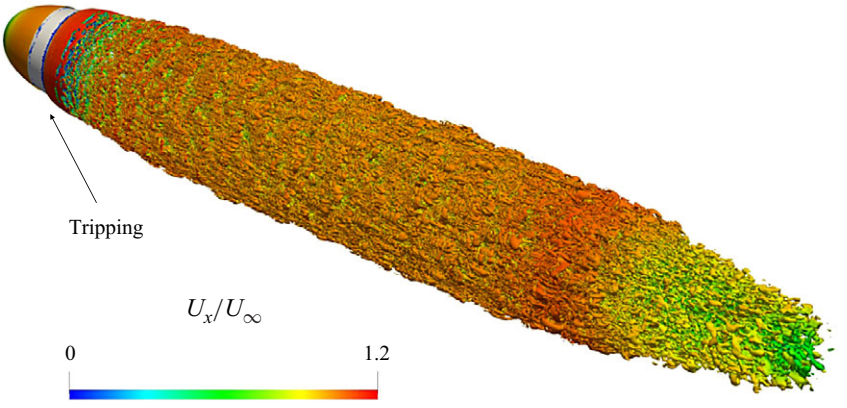

Figure 6. Instantaneous near-wall vortical structures visualised by the Liutex vortex identification method ($\tilde{\Omega}_R = 0.52$). The vortical structures are coloured by instantaneous streamwise velocity normalised by the mean inflow velocity U_∞.

(Kumar & Mahesh 2018) and experimental measurements (Huang *et al.* 1992), validating the accuracy of the present numerical simulation.

3. Overview of flow fields and boundary layer development

3.1. *Overview of the flow fields*

Figure 6 shows the instantaneous three-dimensional vortex structures using the Liutex vortex identification method (Liu *et al.* 2018). Iso-surfaces are extracted at threshold $\tilde{\Omega}_R = 0.52$, with the non-dimensional streamwise velocity used for colouring. The vortex structures illustrate that numerical tripping initiates a rapid transition from laminar to turbulent flow, with near-wall turbulence exhibiting multi-scale characteristics. Along the flow direction, the TBL continuously develops, and the vortex structures attached to the hull grow rapidly, leading to an increase in boundary layer thickness. At the stern, APG induces flow separation, generating a wake region densely populated by vortical structures.

Figure 7 presents the instantaneous flow fields around the SUBOFF model, showcasing both the instantaneous streamwise velocity and pressure distributions. The velocity field highlights concentration of fluctuations within the near-wall boundary layer. In the instantaneous pressure field shown in figure 7(*b*), the stagnation point at the bow corresponds to a high-pressure region, while the stern region is characterised by an APG. The mid-body exhibits a near ZPG, with pronounced pressure fluctuations observed throughout.

3.2. *Boundary layer development*

Building upon the analysis of instantaneous flow fields, we further investigate the development of the TBL. Figure 8 presents the spatial evolution of TBL parameters along the hull. The complex curvature variations in the stern region render traditional methods, such as the 99 % freestream velocity criterion, inadequate for reliably quantifying boundary layer thickness under APG. Recent studies have introduced advanced approaches for boundary layer thickness estimation in flows with curved geometries, such as vorticity-based (Spalart & Watmuff 1993; Coleman, Rumsey & Spalart 2018) and total-pressure-based (Patel, Nakayama & Damian 1974; Griffin, Fu & Moin 2021; He *et al.* 2024*a*) methodologies. This work employs the total-pressure-based method, defining the boundary layer thickness as the location where 99 % of the total pressure $C_{p,total}$ is

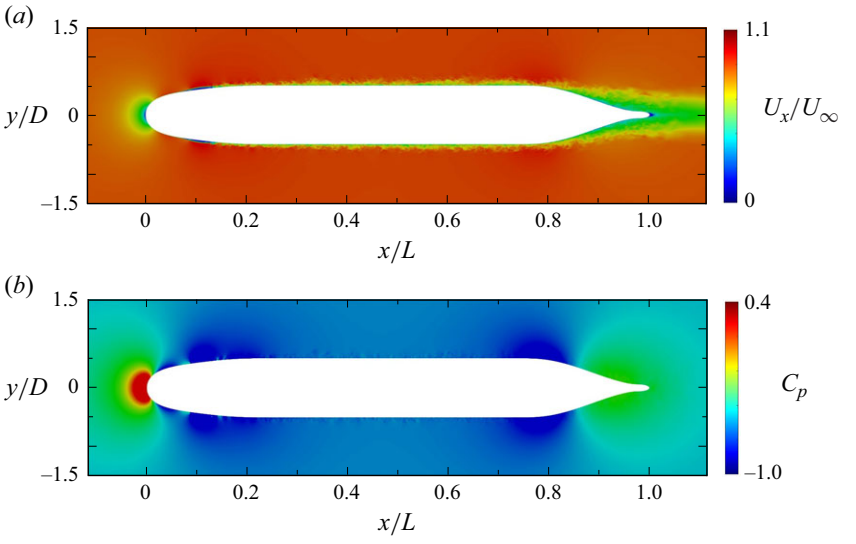

Figure 7. Instantaneous flow field of (*a*) streamwise velocity and (*b*) pressure.

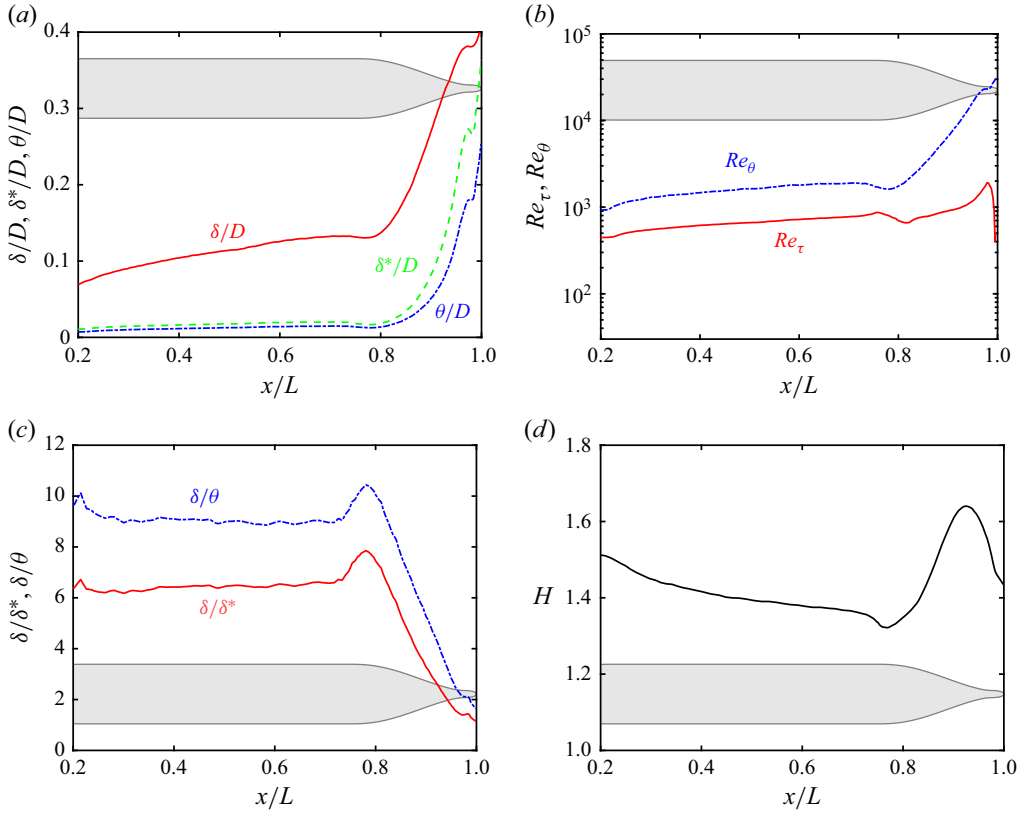

Figure 8. Evolution of TBL parameters along the hull: (*a*) boundary layer thickness δ, displacement thickness δ^* and momentum thickness θ; (*b*) friction Reynolds number Re_τ and momentum thickness Reynolds number Re_θ; (*c*) thickness ratios δ/δ^*, δ/θ, and (*d*) shape factor H.

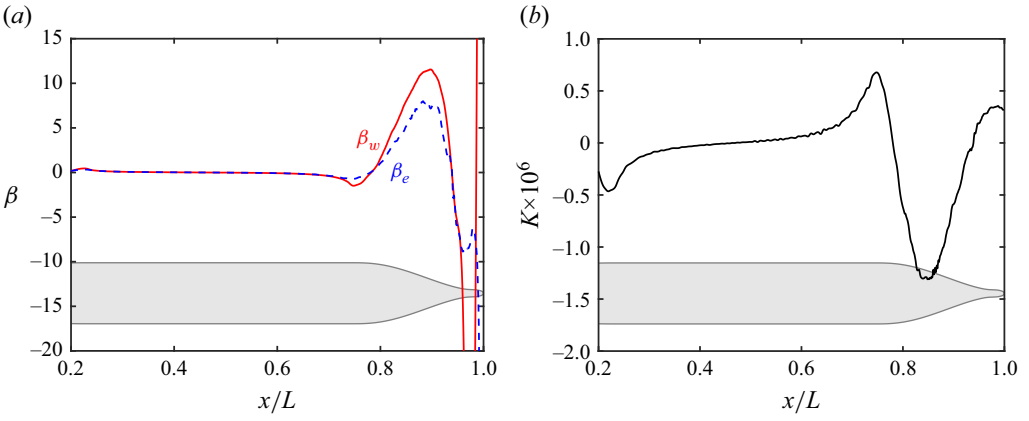

Figure 9. Evolution of (*a*) Clauser pressure gradient parameter β and (*b*) acceleration parameter K along the hull.

recovered. Figure 8(*a*) depicts the distribution of key boundary layer integral parameters, thickness δ, displacement thickness δ^*, and momentum thickness θ along the hull. As the boundary layer evolves downstream, all integral thickness parameters increase monotonically, with accelerated growth under the APG in the stern region. A slight dip is observed at $x/L \approx 0.77$, primarily due to the local FPG. Figure 8(*b*) presents the distribution of local Reynolds numbers, include the friction Reynolds number $Re_\tau = \delta u_\tau/\nu$ and momentum thickness Reynolds number $Re_\theta = \theta U_\infty/\nu$. In addition, the ratios of boundary layer thicknesses δ/δ^*, δ/θ and shape factor $H = \delta^*/\theta$ are shown in figures 8(*c,d*), respectively. All the parameters are highly sensitive to FPG and APG. At the parallel mid-body, H is approximately 1.4, whereas at the stern, H rapidly increases from 1.3 under FPG conditions to nearly 1.7 under APG conditions.

Figure 9 shows the evolution of Clauser pressure gradient parameter β (Clauser 1954) and acceleration parameter K (Kline *et al.* 1967) along the hull, defined as

$$\beta = \frac{\delta^*}{\tau_w}\frac{\mathrm{d}P}{\mathrm{d}x}, \quad K = \frac{\nu}{U_e^2}\frac{\mathrm{d}U_e}{\mathrm{d}x}, \tag{3.1}$$

where the β parameter can be defined using either P_e or P_w, corresponding to the local static pressure at the edge of the boundary layer and on the wall, respectively. Figure 9(*a*) reveals a markedly stronger near-wall pressure gradient compared to that at the boundary layer edge, consistent with the results reported by Morse & Mahesh (2021). The pressure gradient around the SUBOFF model exhibits a complex spatial evolution, with alternating regions of APG and FPG along the hull. Beyond $x/L > 0.3$, the influence of the numerical trip becomes negligible, and a near ZPG is observed over most of the parallel mid-body. Notably, a small FPG region is observed before the APG zone at the stern, approximately within $0.71 < x/L < 0.78$. In this region, the flow accelerates, with the acceleration parameter $K > 0$ peaking at $x/L \approx 0.75$. Due to the FPG, the local boundary layer thickness decreases, as shown in figure 8(*a*). Subsequently, for $0.79 < x/L < 0.94$, the flow experiences a strong APG due to the contraction of the body shape. Beyond $x/L \approx 0.94$, the streamwise concave curvature induces another FPG region.

Figure 10 shows the evolution of transverse curvature parameters δ/r_0 and r_0^+ along the hull. As noted in the Introduction, these parameters govern transverse curvature effects. For large local curvature radius r_0, transverse curvature minimally impacts boundary layer dynamics, primarily influencing the outer layer (Piquet & Patel 1999). For small

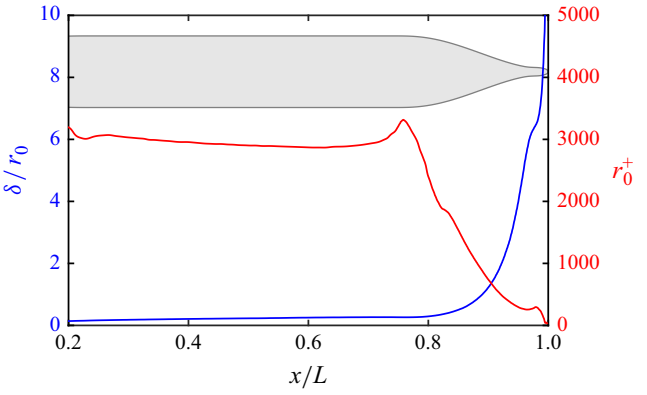

Figure 10. Evolution of transverse curvature parameters (δ/r_0 and r_0^+) along the hull.

r_0, particularly when $\delta/r_0 > 1$, transverse curvature alters TBL behaviour, elevating wall friction (Alam 2020) and attenuating low-frequency wall pressure fluctuations (Neves *et al.* 1994). As the flow develops downstream, δ/r_0 continuously increases. In the FPG region, rising local wall friction drives r_0^+ upwards. Conversely, in the APG region, r_0^+ rapidly decreases.

4. Analysis of wall pressure fluctuations

In this section, we study the spectral and statistical characteristics of wall pressure fluctuations on the SUBOFF model. Due to the lack of publicly available experimental or high-fidelity WRLES data for the SUBOFF model, the predicted results are compared with the WRLES (Cohen & Gloerfelt 2018), DNS (Na & Moin 1998), experimental measurement (Schewe 1983) and empirical models (Goody 2004; Rozenberg *et al.* 2012; Hu & Herr 2016; Lee 2018) for flat-plate TBLs. Figure 11 presents the wall pressure fluctuation frequency spectra at the mid-body of the hull ($x/L = 0.5$). The one-sided power spectral density (PSD) was computed by applying a discrete Fourier transform (DFT) to single-point fluctuating pressure time-history data. To mitigate spectral leakage, the time series (25 600 samples) was divided into three overlapping segments with 50 % overlap, and a Hanning window was applied. The spectra were further smoothed using circumferential averaging across azimuthally equivalent positions on the axisymmetric hull.

As shown in figure 11, the amplitude of wall pressure spectra initially rises with frequency before decaying, exhibiting a characteristic broadband peak. The spectra align closely with DNS (Na & Moin 1998), WRLES (Cohen & Gloerfelt 2018) and experiment (Schewe 1983) data. In the inertial subrange ($\omega\delta^*/U_e \approx 1.5{-}4$), the spectral levels in the present study are slightly lower than those in Cohen & Gloerfelt (2018) due to the smaller Re_θ. At higher frequencies ($\omega\delta^*/U_e > 4$), however, the spectral levels exceed those of Cohen & Gloerfelt (2018), with a slower decay rate. The discrepancy stems from the finer streamwise grid resolution at $x/L = 0.5$, where $\Delta x^+ = 24$, compared to $\Delta x^+ = 37.6$ used by Cohen & Gloerfelt (2018). The reduced grid spacing better resolves high-frequency fluctuations, mitigating numerical dissipation and preserving spectral energy at smaller scales. In terms of empirical spectral models, the current results align most closely with the Goody model (Goody 2004) and Lee model (Lee 2018) in the low-frequency region, while the Hu model (Hu & Herr 2016) shows the poorest agreement. The Rozenberg model (Rozenberg *et al.* 2012) slightly overestimates spectral levels at low frequencies, and underestimates spectral levels at high frequencies, which is consistent with the

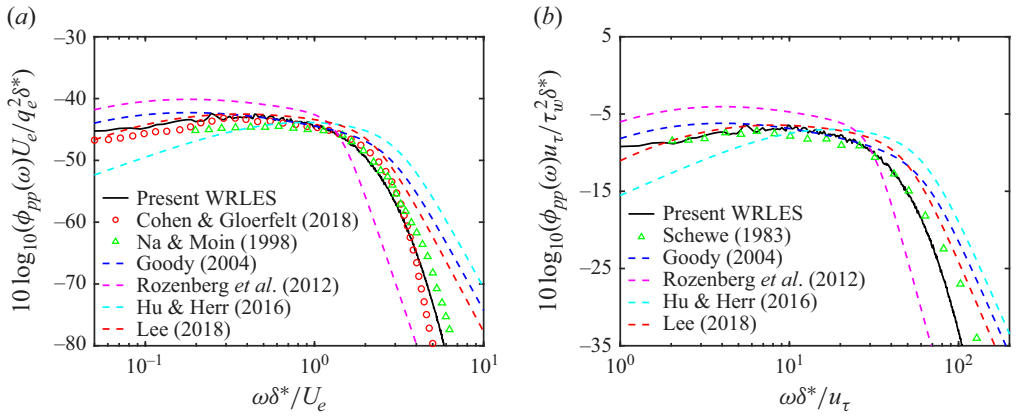

Figure 11. Wall pressure fluctuations frequency spectra at the mid-body of the hull ($x/L = 0.5$). The black solid line represents the results of present WRLES for axisymmetric boundary layers at $Re_\theta = 1631$. The red circles correspond to the WRLES results by Cohen & Gloerfelt (2018) for ZPG flat-plate flow at $Re_\theta = 1693$, while the green triangles in (*a*) and (*b*) represent DNS results by Na & Moin (1998) and experimental measurement by Schewe (1983) for ZPG flat-plate flow at $Re_\theta = 1400$, respectively. The dashed lines in four different colours represent empirical models for flat-plate wall pressure fluctuation spectra.

observations in a previous study (Lee 2018). Furthermore, the high-frequency spectral levels predicted by the LES are systematically lower than those from DNS, experiment and empirical models, attributable to energy loss caused by the SGS model's inherent dissipation.

Based on the validation results, the spatial evolution of wall pressure fluctuations along the hull is analysed in detail. After that, we further investigate the scaling laws and space–time correlations for the non-equilibrium axisymmetric boundary layer under spatially varying pressure gradients, elucidating the interplay between pressure gradients and curvature effects.

4.1. *Evolution of wall pressure fluctuations*

Figure 12 illustrates the streamwise evolution of the wall pressure r.m.s. normalised by reference dynamic pressure q_∞, local dynamic pressure q_e, local wall shear stress τ_w, and local maximum magnitude of Reynolds shear stress τ_{max}. Here, $q_\infty = 0.5\rho U_\infty^2$ and $q_e = 0.5\rho U_e^2$, and τ_{max} is defined as

$$\tau_{max} = -\rho\langle u_s u_n\rangle_{max}, \tag{4.1}$$

where u_s and u_n are obtained from axial velocity u_x and radial velocity u_r through the coordinate transformation

$$u_s = u_x\cos\alpha - u_r\sin\alpha, \quad u_n = u_x\sin\alpha + u_r\cos\alpha, \tag{4.2}$$

in which s and n represent the tangential and normal directions relative to the wall, respectively, and α is the angle between the wall tangential direction and the axial direction of SUBOFF.

As the flow moves downstream, the r.m.s. of the wall pressure fluctuations follows a non-monotonic trend, characterised by an initial decrease, followed by an increase, and a subsequent decrease. When normalised by q_e, the r.m.s. values diminish more sharply in FPG regions but amplify more rapidly in APG regions. This behaviour stems from competing mechanisms: FPG suppresses wall pressure fluctuations while increasing outer

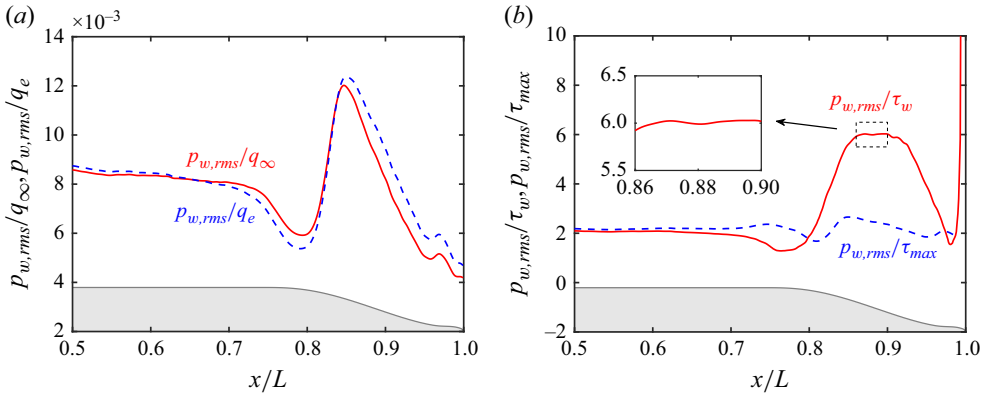

Figure 12. Wall pressure r.m.s. values normalised by: (*a*) reference dynamic pressure q_∞ and local dynamic pressure q_e; (*b*) local wall shear stress τ_w and local maximum magnitude of Reynolds shear stress τ_{max}.

edge velocity U_e, whereas APG intensifies wall pressure fluctuations while reducing U_e. Consequently, q_e proves suboptimal for scaling wall pressure fluctuations under spatially varying pressure gradients.

In contrast, the wall shear stress τ_w appears to be a more effective scaling parameter for wall pressure fluctuations. For a flat-plate TBL, the ratio $p_{w,rms}/\tau_w$ increases monotonically with Re_τ. Prior studies (Farabee & Casarella 1991; Abe, Matsuo & Kawamura 2005; Cohen & Gloerfelt 2018) established an empirical relationship for ZPG flows:

$$\left(p_{w,rms}/\tau_w\right)^2 = 6.5 + 1.86\ln(Re_\tau/333), \tag{4.3}$$

suggesting Reynolds number dependence. However, in the aft section of the parallel mid-body ($0.5 < x/L < 0.7$), the ratio $p_{w,rms}/\tau_w$ does not exhibit a slight increase with Re_τ. Instead, it remains approximately constant at 2.1. This behaviour can be attributed to the influence of a mild FPG. As shown in figure 9, the Clauser pressure gradient parameter β slightly decreases in the range $0.5 < x/L < 0.7$, while the acceleration parameter K gradually increases. Additionally, it is noteworthy that the value $p_{w,rms}/\tau_w \approx 2.1$ over the parallel mid-body is slightly lower than experimental observations of ZPG TBL in the corresponding Reynolds number range (Sillero, Jiménez & Moser 2013), which can be attributed to the influence of transverse curvature. As discussed in the Introduction, transverse curvature effects can lead to increased wall shear stress and a slight suppression of wall pressure fluctuations.

In the range $0.86 < x/L < 0.9$, $p_{w,rms}$ and τ_w decline concurrently, stabilising at a plateau $p_{w,rms}/\tau_w \approx 6$. As shown in figure 9, this plateau corresponds to the APG-dominant regime, where β_e peaks before decreasing. The streamwise curvature is approximately zero, and the pressure gradient remains relatively stable in this region. A similar trend was observed experimentally by Balantrapu *et al.* (2023) for flow over BOR under APG. In their study, the stern region of the BOR experienced a nearly uniform APG without streamwise curvature, resulting in $p_{w,rms}/\tau_w \approx 7$. They concluded that wall-friction-induced motion remains a dominant contributor to pressure fluctuations in attached flows, even under strong APG. The present numerical results align with this observation, though the simulated ratio $p_{w,rms}/\tau_w \approx 6$ is slightly lower than the experimental value. Two factors can explain this discrepancy: the Reynolds number effects and the pressure gradient strength. The Reynolds number $Re_L = 1.1 \times 10^6$ in the study is lower than the experimental $Re_L = 1.8 \times 10^6$. The local friction Reynolds number

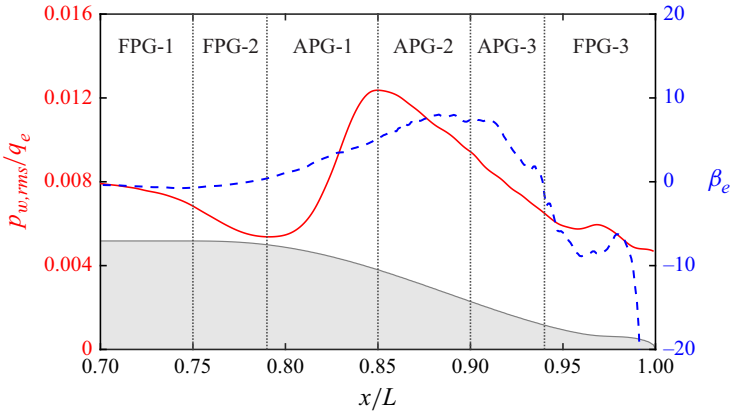

Figure 13. Schematic diagram of the flow region division at the stern.

Re_τ is also smaller. Moreover, the APG in this study ($\beta_e = 6-8$) is weaker than in the experiments ($\beta_e = 11-16$). For axisymmetric APG flows, $p_{w,rms}/\tau_w$ can correlate with the local pressure gradient parameters (such as β_e), reflecting the boundary layer's proximity to equilibrium. As noted by Cohen & Gloerfelt (2018), equilibrium boundary layers require a near-constant streamwise pressure gradient to achieve self-similarity, enabling scaling via τ_w. However, the relationship $p_{w,rms}/\tau_w \approx 6$ breaks down when streamwise curvatures and strong streamwise pressure gradient variations present. In non-equilibrium flows (e.g. $0.79 < x/L < 0.85$, where β_e increases rapidly), $p_{w,rms}/\tau_w$ rises sharply from 1.5 to 6. Beyond $x/L > 0.9$, transverse and concave streamwise curvature effects cause β_e to decrease abruptly, reducing $p_{w,rms}/\tau_w$.

Among the three pressure scaling parameters, the local maximum magnitude of the Reynolds shear stress τ_{max} appears to be the most effective scaling parameter for wall pressure fluctuations. As discussed in the Introduction, prior studies (Simpson *et al.* 1987; Na & Moin 1998; Abe 2017; Schatzman & Thomas 2017) have highlighted the significant role of the turbulent shear term in governing wall pressure fluctuations within APG TBLs. These works proposed scaling wall pressure fluctuations using the maximum turbulent shear stress under APG conditions. However, the flow in the present configuration demonstrates greater complexity due to the continuous variation in streamwise curvature along the stern part, which includes both convex and concave curvatures. This curvature variation is further coupled with an evolving transverse curvature. In the APG region without streamwise curvature ($0.86 < x/L < 0.9$), τ_w is demonstrated to be an effective scaling parameter. However, across the entire APG region ($0.79 < x/L < 0.94$), the variation in $p_{w,rms}/\tau_{max}$ (ranging from 1.7 to 2.7) is significantly smaller compared to $p_{w,rms}/q_e$ (ranging from 0.0053 to 0.0124) and $p_{w,rms}/\tau_w$ (ranging from 1.5 to 6).

Due to the coexistence of convex and concave streamwise curvatures, the flow in the stern region features alternating zones of FPGs and APGs. To facilitate systematic analysis, based on the pressure gradient distribution in figure 9 and the r.m.s. of the wall pressure fluctuations in figure 12, the stern boundary layer is further divided into six distinct regions, as shown in figure 13.

(i) FPG-1 ($0.71 < x/L < 0.75$): the flow gradually transitions from ZPG to FPG, reaching the peak of the FPG at $x/L \approx 0.75$.

(ii) FPG-2 ($0.75 < x/L < 0.79$): the FPG gradually decreases and returns to the ZPG at $x/L \approx 0.79$.
(iii) APG-1 ($0.79 < x/L < 0.85$): this region is characterised by convex streamwise curvature, where the flow transitions from ZPG to APG.
(iv) APG-2 ($0.85 < x/L < 0.90$): the streamwise curvature is unchanged, with the wall pressure r.m.s. and wall shear stress exhibiting a linear relationship, i.e. $p_{w,rms}/\tau_w \approx 6$.
(v) APG-3 ($0.90 < x/L < 0.94$): the flow is approaching a concave streamwise curvature, with APG gradually decreasing and eventually returning to ZPG.
(vi) FPG-3 ($0.94 < x/L < 0.99$): due to the change in streamwise curvature, the flow transitions back to FPG again, with flow separation occurring very close to the stern.

Figure 14 illustrates the evolution of wall pressure fluctuations frequency spectra at the stern, normalised by reference pressure $p_{ref} = 20$ μPa, with the fluid density specified as $1.225\,\mathrm{kg\,m^{-3}}$. The inset displays the corresponding pre-multiplied spectra $\omega\,\phi_{pp}(\omega)$, where the x-axis employs a logarithmic scale, and the y-axis uses a linear scale. This ensures that the area under the pre-multiplied curve corresponds to the total energy of wall pressure fluctuations. Figure 15 further visualises the spatially continuous pre-multiplied power spectra as contour plots, highlighting their temporal and spatial evolution. In figure 14(*a*), a mild strengthening of the FPG correlates with a modest reduction in spectral levels at low-to-mid frequencies ($\omega < 1000\,\mathrm{rad\,s^{-1}}$), and a slight elevation at high frequencies ($\omega > 1000\,\mathrm{rad\,s^{-1}}$). This trend suggests that stronger FPG suppresses large-scale turbulent structures while amplifying small-scale fluctuations. In figure 14(*b*), as the FPG weakens and transitions toward a ZPG in region FPG-2, spectral levels decrease uniformly across all frequencies.

Subsequently, the TBL encounters a strong APG induced by the convex streamwise curvature. While prior studies (Na & Moin 1998; Rozenberg *et al.* 2012; Cohen & Gloerfelt 2018; Lee 2018) have examined the isolated effects of APG on wall pressure fluctuations, conclusively demonstrating that APG amplifies low-frequency energy and attenuates high-frequency components, the dynamic evolution of APG (emerges, intensifies and decays) in this work reveals a more nuanced response. As shown in figures 14(*c*) and 14(*d*), the spectra exhibit a distinct two-stage evolution: a sharp rise in low- and mid-frequency energy during APG onset, followed by progressive attenuation of mid- and high-frequency energy as the APG stabilises. In the APG-1 region, the parameter β_e increases rapidly from 1.05 to 5.2. Correspondingly, figure 14(*c*) reveals a sharp escalation in the low- and mid-frequency spectral energy ($\omega < 1000\,\mathrm{rad\,s^{-1}}$), while the attenuation of high-frequency components ($\omega > 1000\,\mathrm{rad\,s^{-1}}$) remains relatively subdued at this stage. However, as β_e reaches its peak and gradually begins to decline, a rapid reduction in spectral energy emerges across the mid- and high-frequency range ($\omega > 150\,\mathrm{rad\,s^{-1}}$), consistent with experimental observations (Balantrapu *et al.* 2023).

In the APG-3 region, as shown in figure 14(*e*), β_e gradually decreases due to the introduction of concave streamwise curvature. A decay in wall pressure fluctuations is observed across the entire frequency range. Notably, the reduction of APG does not lead to a replenishment of high-frequency spectral levels, which can be attributed to the shifting of turbulent structure away from the wall. This phenomenon will be further discussed later. Downstream in the FPG-3 region, shown in figure 14(*f*), the concave streamwise curvature locally enhances the FPG, accelerating the flow and amplifying high-frequency wall pressure fluctuations through increased small-scale turbulence production. Eventually, flow separation occurs beyond $x/L > 0.99$ as the streamwise curvature transitions from concave to convex.

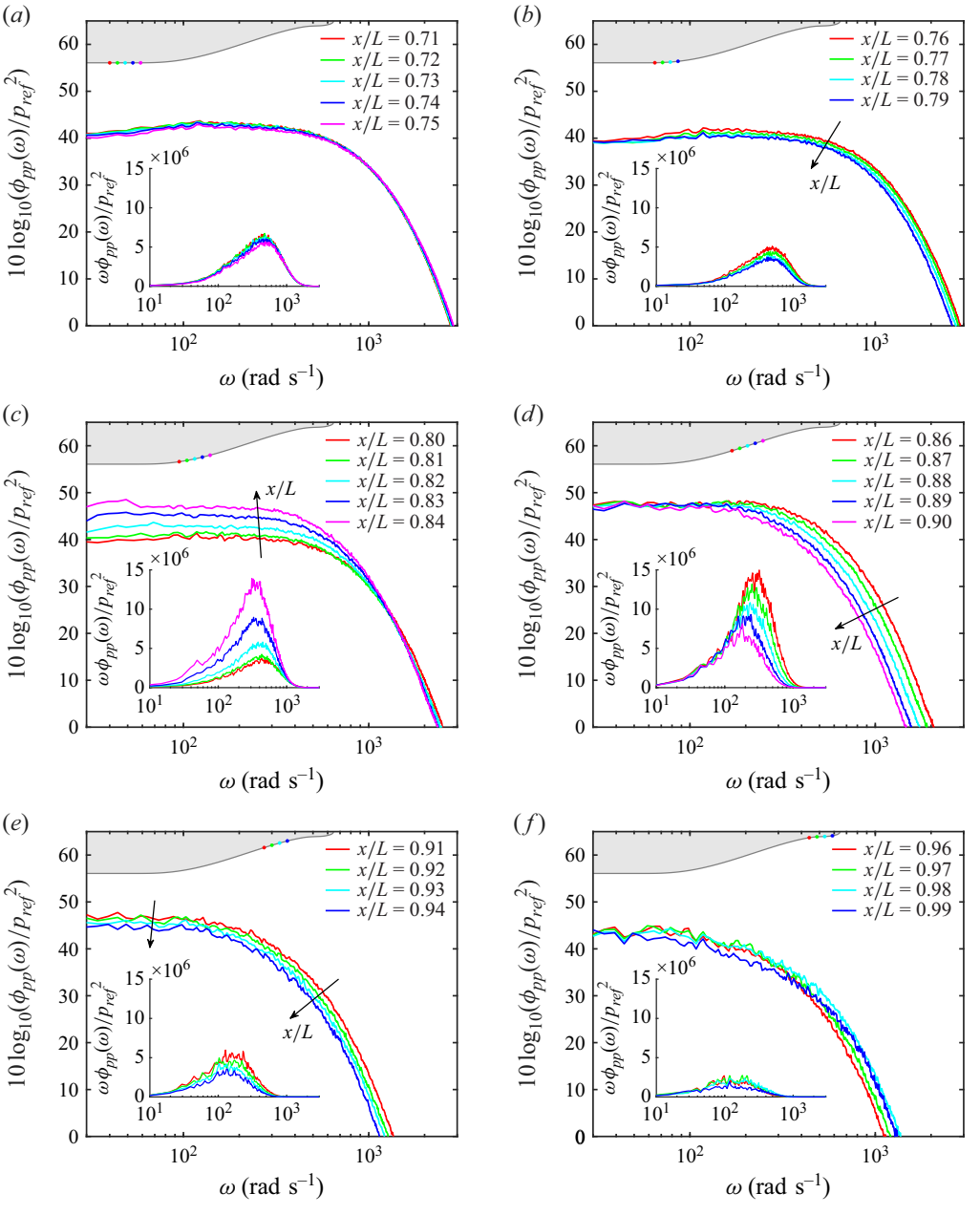

Figure 14. Evolution of wall pressure fluctuation frequency spectra at the stern: (*a*) FPG-1, (*b*) FPG-2, (*c*) APG-1, (*d*) APG-2, (*e*) APG-3, (*f*) FPG-3. The inset shows corresponding pre-multiplied form $\omega\,\phi_{pp}(\omega)$. The SUBOFF model and probe locations are displayed at the top.

4.2. *Scaling laws of wall pressure fluctuations*

To identify the dominant contributors to wall pressure fluctuations across different frequency bands, it is critical to examine the scaling law governing these fluctuations in axisymmetric boundary layers with varying pressure gradient. Over the past few decades, numerous scaling approaches (Schloemer 1966; Choi & Moin 1990; Farabee & Casarella 1991; Keith *et al.* 1992; Na & Moin 1998) have been proposed. However, owing to

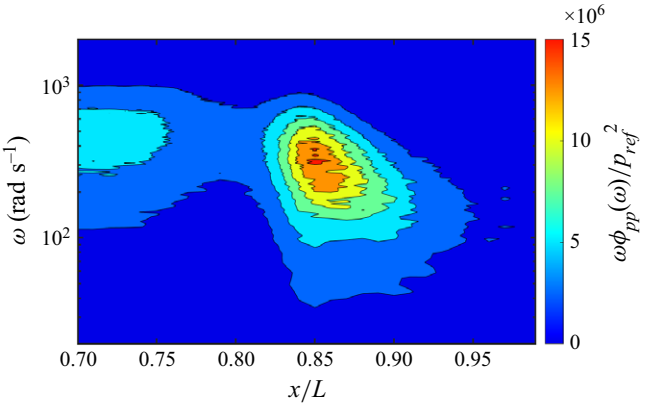

Figure 15. Contour of wall pressure fluctuations pre-multiplied energy frequency spectra at the stern.

the multi-scale nature of turbulence, no universal scaling law has been established that achieves consistent collapse across all frequency ranges.

Figure 16 illustrates the non-dimensional PSD of wall pressure fluctuations under different scaling methods in the stern region. Six common scaling methods have been examined: outer scaling (q_e, δ and U_e), inner scaling (τ_w, δ_v and u_τ), mixed scaling (τ_w, δ and U_e), Zagarola–Smits scaling (τ_w, δ^2/δ^* and U_e), Reynolds shear stress scaling (τ_{max}, δ and U_e), and displacement thickness scaling (τ_{max}, δ^* and U_e). As shown in figure 14, the wall pressure spectra exhibit a generally monotonic trend within each flow region. Therefore, we select the start and end points of each region for comparison, which better highlights the variation of wall pressure fluctuations across different stern regions under various scaling laws. Figure 16 clearly illustrates that when both varying streamwise and transverse curvatures are present, conventional inner or mixed scaling methods completely fail. Among all the scaling approaches, normalisation using the local maximum Reynolds shear stress yields the best collapse, consistent with the trend observed in figure 12. Across the entire stern region, the variation of $p_{w,rms}/\tau_{max}$ is minimal. This underscores the pivotal role of τ_{max} in governing wall pressure fluctuations, particularly in non-equilibrium boundary layers. Notably, the Zagarola–Smits scaling performs poorly in the stern region of the SUBOFF model, primarily because δ and δ^* are not equivalent length scales, as their ratio varies with the pressure gradient parameter β_e (figure 8*c*). Compared to the displacement thickness δ^* scaling (figure 16*f*), the boundary layer thickness δ (figure 16*e*) is clearly a more effective scaling parameter.

Figure 17 illustrates the non-dimensional PSD of wall pressure fluctuations under different scaling methods in the APG-2 region ($0.85 < x/L < 0.90$). In this region, the streamwise curvature is approximately zero, and the r.m.s. wall pressure exhibits a linear relationship with the wall shear stress, specifically $p_{w,rms}/\tau_w \approx 6$. This relationship closely resembles the experimental results studied by Balantrapu *et al.* (2023) in their BOR experiment. Among the selected scaling methods, the mixed scaling (τ_w, δ and U_e) achieves an excellent collapse of the wall pressure fluctuation spectra across the entire frequency range. This finding is in complete agreement with the experimental conclusions of Balantrapu *et al.* (2023), confirming τ_w, δ and U_e as the optimal scaling parameters in this flow regime. Notably, the scaling retains its effectiveness within the viscous region (figure 17*b*), consistent with experimental observations. The viscous time scale ν/u_τ^2 exhibits dependence on the outer time scale δ/U_e, suggesting coupling between inner viscous dynamics and outer flow scales. Additionally, scaling using the local maximum

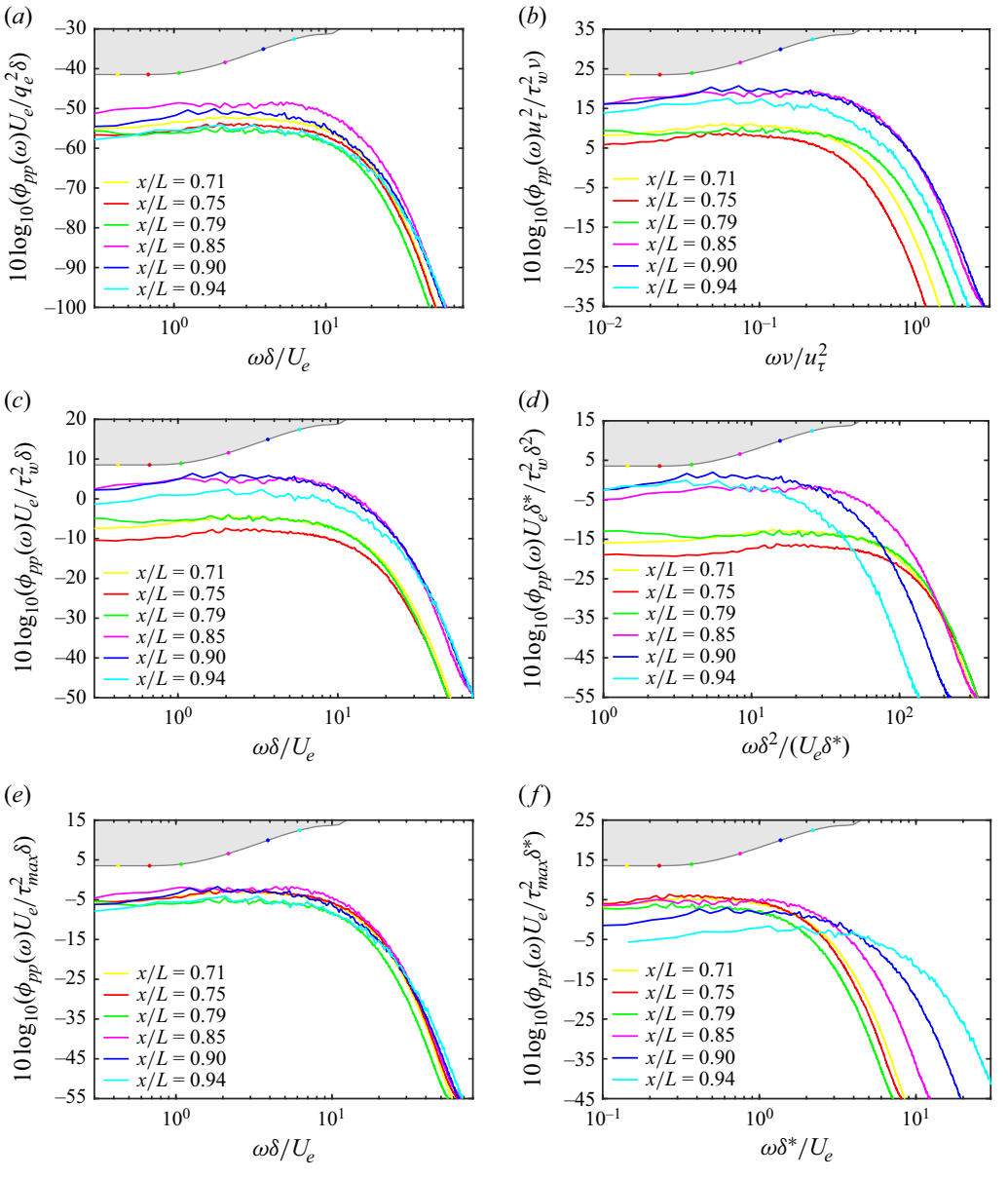

Figure 16. Non-dimensional PSD of wall pressure fluctuations under different scaling methods: (*a*) outer scaling (q_e, δ and U_e); (*b*) inner scaling (τ_w, δ_v and u_τ); (*c*) mixed scaling (τ_w, δ and U_e); (*d*) Zagarola–Smits scaling (τ_w, δ^2/δ^* and U_e); (*e*) Reynolds shear stress scaling (τ_{max}, δ and U_e); (*f*) displacement thickness scaling (τ_{max}, δ^* and U_e).

magnitude of the Reynolds shear stress τ_{max} (figure 17*e*) also collapses the spectra across the entire frequency range.

Figures 14 and 15 demonstrate that the strong APG at the stern drives abrupt changes in the wall pressure fluctuation spectra within localised regions. In the APG-1 region shown in figure 14(*c*), the low-frequency component of wall pressure fluctuations increases sharply by approximately 10 dB, while the APG-3 region exhibits a broadband reduction in spectral energy levels across all frequencies. For the two APG regions, we also conducted

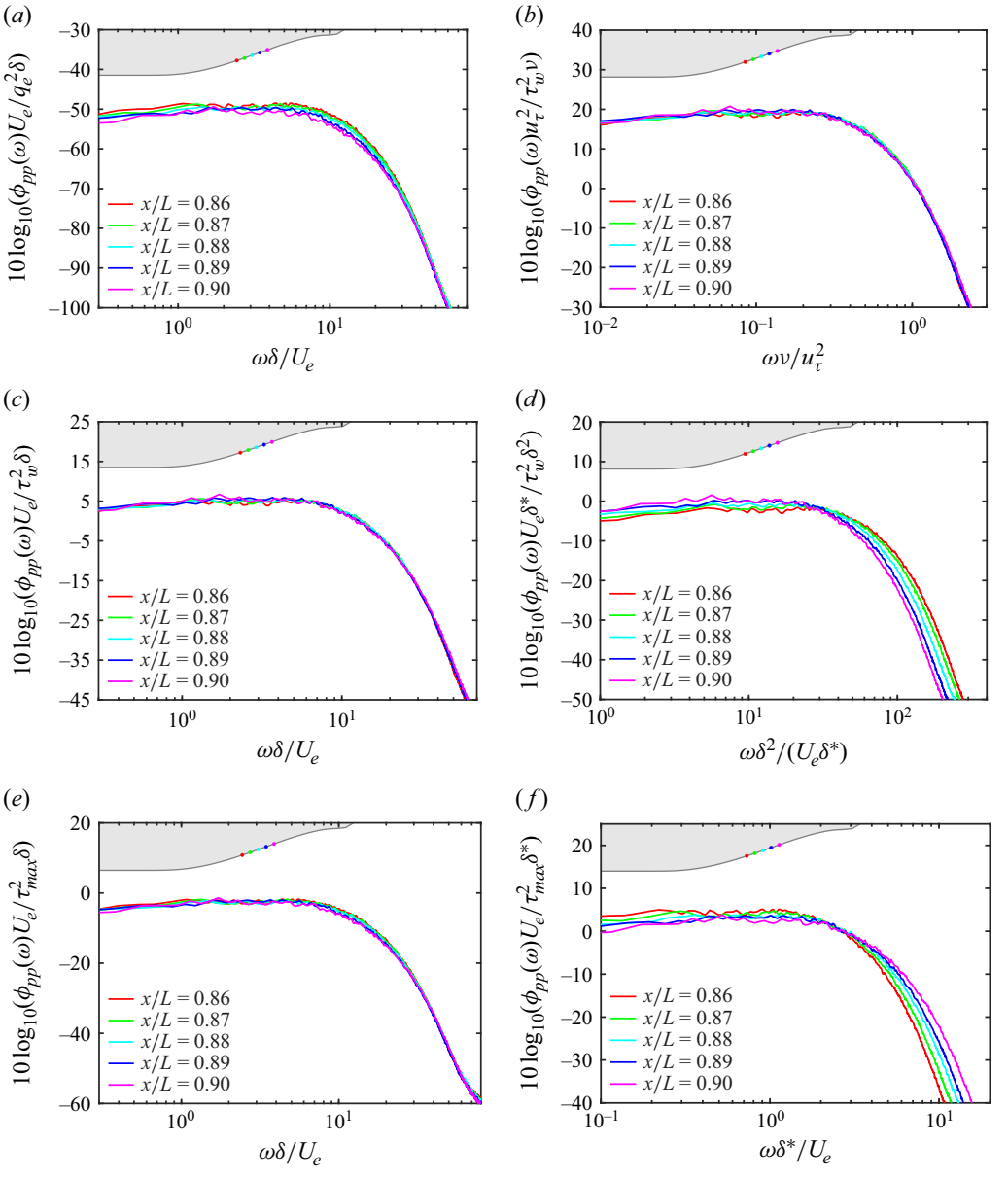

Figure 17. Non-dimensional PSD of wall pressure fluctuations under different scaling methods in the APG-2 region ($0.85 < x/L < 0.90$): (*a*) outer scaling (q_e, δ and U_e); (*b*) inner scaling (τ_w, δ_v and u_τ); (*c*) mixed scaling (τ_w, δ and U_e); (*d*) Zagarola–Smits scaling (τ_w, δ^2/δ^* and U_e); (*e*) Reynolds shear stress scaling (τ_{max}, δ and U_e); (*f*) displacement thickness scaling (τ_{max}, δ^* and U_e).

additional and detailed comparisons of these scaling methods in Appendix B. The results further confirm the significant advantage of scaling based on the Reynolds shear stress.

4.3. *Space–time characteristics of wall pressure fluctuations*

Since turbulence is a spatiotemporal coupled problem, performing a one-dimensional spectral analysis of wall pressure fluctuations solely in the time domain inevitably results

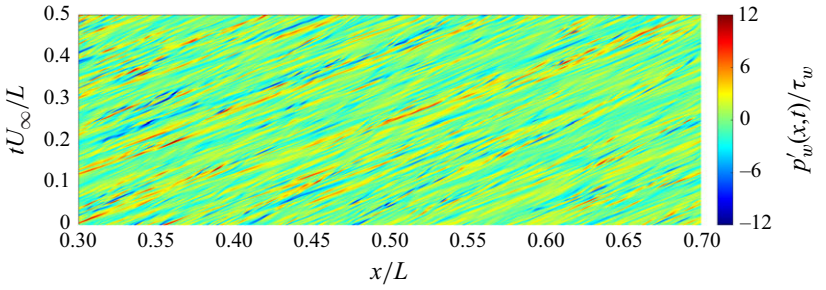

Figure 18. Space–time contours of wall pressure fluctuations along the streamwise direction in the mid-body region ($x/L = 0.3-0.7$) of the hull.

in the loss of spatial information. In this subsection, we investigate the space–time characteristics of wall pressure fluctuations by analysing their wavenumber–frequency spectra and space–time correlation functions. Analysing wavenumber–frequency spectra typically requires the assumption of streamwise uniformity. However, the flow over the SUBOFF stern exhibits significant streamwise pressure gradient variations. The APG boundary layers, in particular, are strongly influenced by upstream flow history (Bobke *et al.* 2017) and the specific manner of gradient application, complicating direct comparisons with datasets derived from simpler configurations. To mitigate this, our wavenumber–frequency spectral analysis is restricted to the parallel mid-body section, where the conventional assumption of negligible streamwise boundary layer thickening remains valid.

Figure 18 presents the space–time contour (spanning half the flow-past time) of wall pressure fluctuations along the streamwise direction in the mid-body region ($x/L = 0.3-0.7$) of the hull. The fluctuations are normalised by the wall shear stress τ_w. The contours reveal alternating high- and low-pressure regions, clearly illustrating the convection and distortion of vortical structures. According to Taylor's frozen-flow hypothesis (Taylor 1938), the 'world lines' of these pressure fluctuations should form perfectly straight trajectories. However, significant deviations from this idealised behaviour are evident, arising from random sweeping effects (Kraichnan 1964; Tennekes 1975) caused by large-scale structures and nonlinear interactions among small-scale turbulent motions.

To compute the wavenumber–frequency spectra of wall pressure fluctuations, a standard methodology involves deploying a streamwise-aligned array of pressure probes to capture space–time fluctuating pressure signals. These signals are stored in a two-dimensional matrix $p(x = m\Delta X, t = n\Delta T)$, where $m = 1, 2, 3, \ldots, M$ and $n = 1, 2, 3, \ldots, N$. Here, ΔX denotes the spatial interval between adjacent probes, and ΔT represents the temporal sampling interval. In this study, the probe spacing ΔX matches the computational grid resolution, while ΔT corresponds to the simulation time step. The acquired pressure data (25 600 time steps) are segmented into 19 overlapping blocks with 50 % overlap to enhance statistical convergence. To mitigate spectral leakage, each segment is multiplied by a Hanning window. Four independent probe arrays, spaced uniformly along the streamwise direction, are circumferentially averaged to improve signal-to-noise ratios. The windowed space–time signals are then transformed into the wavenumber–frequency domain via a two-dimensional discrete Fourier transform:

$$\hat{p}(k_x, \omega) = \frac{\sqrt{8/3}}{MN} \sum_{m=1}^{M} \sum_{n=1}^{N} w(n\Delta T)\ \ p(m\Delta X, n\Delta T) \times \exp^{-\mathrm{i}(m\Delta X\, k_x - n\Delta T\, \omega)}, \qquad (4.4)$$

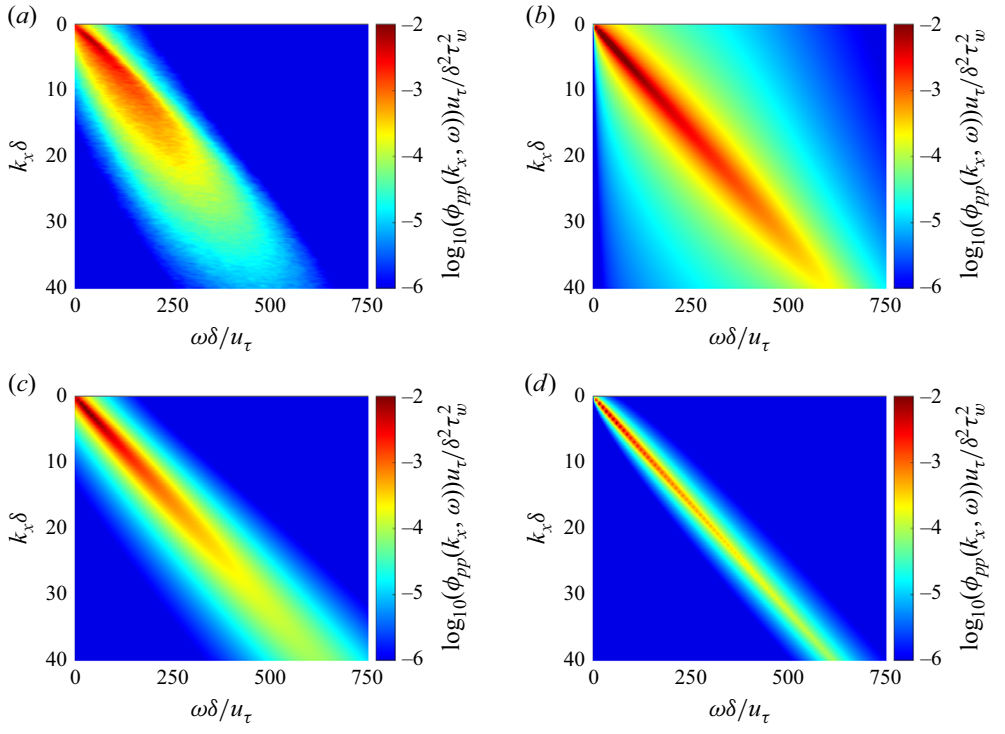

Figure 19. (*a*) Wavenumber–frequency spectra of wall pressure fluctuations at mid-body ($x/L = 0.3-0.7$) of SUBOFF, for present WRLES. The result is compared with semi-empirical models for the flat-plate TBL: (*b*) Corcos model; (*c*) Chase I model; (*d*) Witting model.

where the factor $\sqrt{8/3}$ compensates for the amplitude attenuation induced by the Hanning window $w(t)$, preserving the r.m.s. value of p. The wavenumber–frequency spectrum $\phi_{pp}(k_x, \omega)$ is obtained by ensemble-averaging the squared Fourier coefficients:

$$\phi_{pp}(k_x, \omega) = \frac{\overline{\hat{p}(k_x, \omega)\ \hat{p}^*(k_x, \omega)}}{\Delta k_x \Delta\omega}, \tag{4.5}$$

where $\Delta k_x = 2\pi/(M\Delta X)$ and $\Delta\omega = 2\pi/(N\Delta T)$ define the streamwise wavenumber and frequency resolutions, respectively. This procedure fully maps the fluctuating pressure field from the space–time domain to the wavenumber–frequency domain.

Figure 19 presents the two-dimensional wavenumber–frequency spectra of wall pressure fluctuations in the mid-body region ($x/L = 0.3-0.7$) of the hull. The results are compared with semi-empirical wavenumber–frequency spectral models for flat-plate TBLs (Corcos 1964; Chase 1980; Witting 1986). The details of these models are provided in Appendix C. Similar to one-dimensional spectral models, wavenumber–frequency spectral models also require mean boundary layer parameters as inputs. Notably, the Corcos model (Corcos 1964) additionally depends on a self-spectral model. In this study, the Goody model (Goody 2004) is selected as the input for the Corcos model. Due to the central symmetry of the wavenumber–frequency spectrum, only the first quadrant ($\omega > 0$, $k_x > 0$) is shown. Figure 19(*a*) reveals that spectral energy at any frequency concentrates near the convection wavenumber k_c, forming a distinct 'convective ridge'. Contrary to Taylor's frozen-flow hypothesis (Taylor 1938), the convective ridge broadens with increasing frequency and wavenumber – a phenomenon termed Doppler broadening. The spectral widening reflects

the distortion of turbulent eddies, driven by the random sweeping effects of large-scale structures on small-scale eddies and nonlinear interactions among the small-scale eddies. Additionally, the highest spectral energy resides in the low-frequency, low-wavenumber regime, decaying continuously with increasing ω and k_x, in agreement with experimental (Abraham & Keith 1998), DNS (Choi & Moin 1990; Yang & Yang 2022), LES (Francis *et al.* 2023; Fan *et al.* 2024*b*) and semi-empirical (Corcos 1964; Chase 1980; Witting 1986) results. A notable feature is the contraction of spectral contours towards $(k_x, \omega) = (0, 0)$ as k_x approaches zero. This behaviour, linked to the rapid source term in the pressure Poisson equation (Yang & Yang 2022), indicates that the wall pressure spectrum initially rises and then declines with increasing k_x – a trend consistent with the one-dimensional spectra in figure 11.

The comparison in figure 19 demonstrates that the high-frequency, high-wavenumber regions of the wavenumber–frequency spectrum from the present WRLES exhibit lower spectral levels than those predicted by semi-empirical models. As noted earlier, this discrepancy stems primarily from streamwise grid resolution limitations and the dissipative effects of the SGS model. Among the three models, the Corcos model (Corcos 1964) significantly overestimates spectral energy away from the convective ridge, likely due to its simplified treatment of spatiotemporal decorrelation mechanisms. Conversely, the Witting model (Witting 1986) underestimates the spectral width, failing to adequately capture the random sweeping effects and distortion dynamics of small-scale eddies. In contrast, the Chase I model (Chase 1980) shows the closest agreement with the WRLES results, accurately reproducing both the convective characteristics and spectral broadening trends of the wall pressure fluctuations.

To enable quantitative comparison of the wavenumber–frequency spectra, figure 20 shows wavenumber-dependent spectral slices at selected frequencies $\omega\delta/(u_\tau = 100, 150, 200, 250)$ in wavenumber–frequency spectra. The comparison reveals that all three semi-empirical models accurately predict the convective peak locations across these frequency bands. Among them, the Chase I model (Chase 1980) shows the closest agreement with the present WRLES results, particularly in the low-wavenumber regime. Notably, the convective ridge in the WRLES spectra exhibits asymmetry about the peak – a feature consistent with prior observations in flat-plate TBLs and turbulent channel flows (Abraham & Keith 1998; Viazzo, Dejoan & Schiestel 2001; Francis *et al.* 2023; Fan *et al.* 2024*b*). In summary, transverse curvature effects exert minimal influence on wall pressure fluctuations in the parallel mid-body region compared to flat-plate configurations. Consequently, the Chase I model remains applicable for rapid prediction of wavenumber–frequency spectra in this region, offering practical utility for engineering applications.

Another point worth noting is the convection velocity U_c of wall pressure fluctuations, which is the slope of the convective ridge in the wavenumber–frequency spectra, defined as (Wills 1971)

$$U_c(\omega) = \omega/k_c(\omega), \tag{4.6}$$

where k_c is the convection wavenumber, and

$$\left(\frac{\partial \phi_{pp}(k_x, \omega)}{\partial k_x}\right)_{k_x = k_c(\omega)} = 0. \tag{4.7}$$

Figure 21 shows the frequency-dependent convection velocity of wall pressure fluctuation. The results are compared with experiment measurement (Abraham & Keith 1998) and the Smol'yakov model (Smol'yakov 2006) for a flat-plate TBL. The model

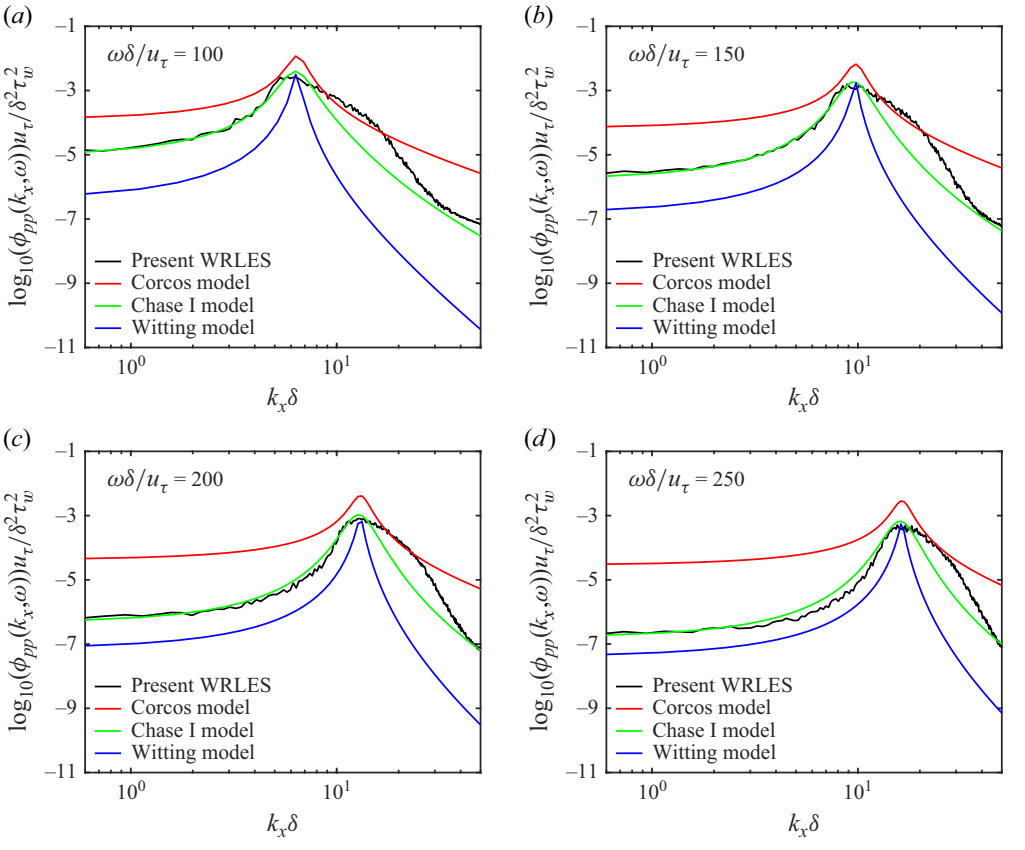

Figure 20. Wavenumber-dependent spectra of wall pressure fluctuations at various frequencies: (*a*) $\omega\delta/u_\tau = 100$, (*b*) $\omega\delta/u_\tau = 150$, (*c*) $\omega\delta/u_\tau = 200$, (*d*) $\omega\delta/u_\tau = 250$.

expression is given as

$$\frac{U_c}{U_\infty} = \frac{1.6(\omega\delta^*/U_\infty)}{1 + 16(\omega\delta^*/U_\infty)^2} + 0.6. \tag{4.8}$$

The convection velocity of present WRLES reaches its peak at $\omega\delta^*/U_\infty = 0.3$. Then, as frequency increases, the convection velocity decreases from approximately $0.8U_\infty$ at low frequencies to $0.7U_\infty$ at high frequencies, consistent with flat-plate TBL studies (Abraham & Keith 1998; Smol'yakov 2006).

Figure 22 presents contour plots of the space–time correlation functions of wall pressure fluctuations at key streamwise locations. Spatial separation is normalised by the freestream velocity U_∞ and boundary layer thickness δ_{mid} at the parallel mid-body ($x/L = 0.5$). The space–time correlation function is defined as

$$R_{pp}(s,\, t,\, \Delta s,\, \Delta t) = \frac{\overline{\langle p'(s,\, t)\; p'(s + \Delta s,\, t + \Delta t)\rangle}}{\sqrt{\langle p'^2(s,\, t)\rangle}\sqrt{\langle p'^2(s + \Delta s,\, t + \Delta t)\rangle}}, \tag{4.9}$$

where Δs and Δt are the streamwise spatial and temporal separations, respectively. The convection velocity of wall pressure fluctuations is derived from the slope $\mathrm{d}(\Delta s)/\mathrm{d}(\Delta t)$. Figures 22(*a–f*) correspond to the ZPG, the FPG, the onset of the APG region, the peak of the APG region, the decline of the APG region, and the end of the APG region,

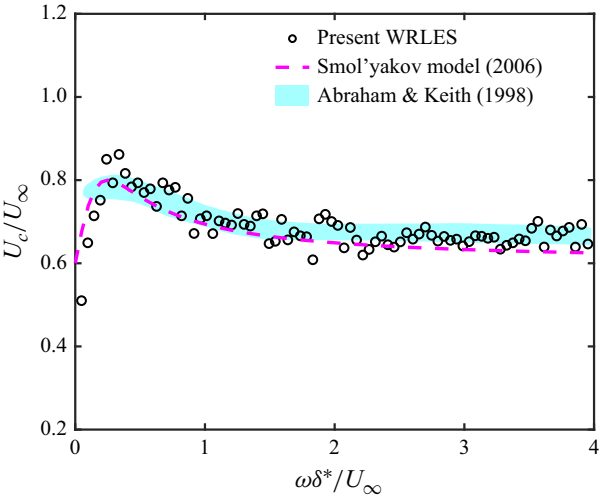

Figure 21. Frequency-dependent convection velocity of wall pressure fluctuations.

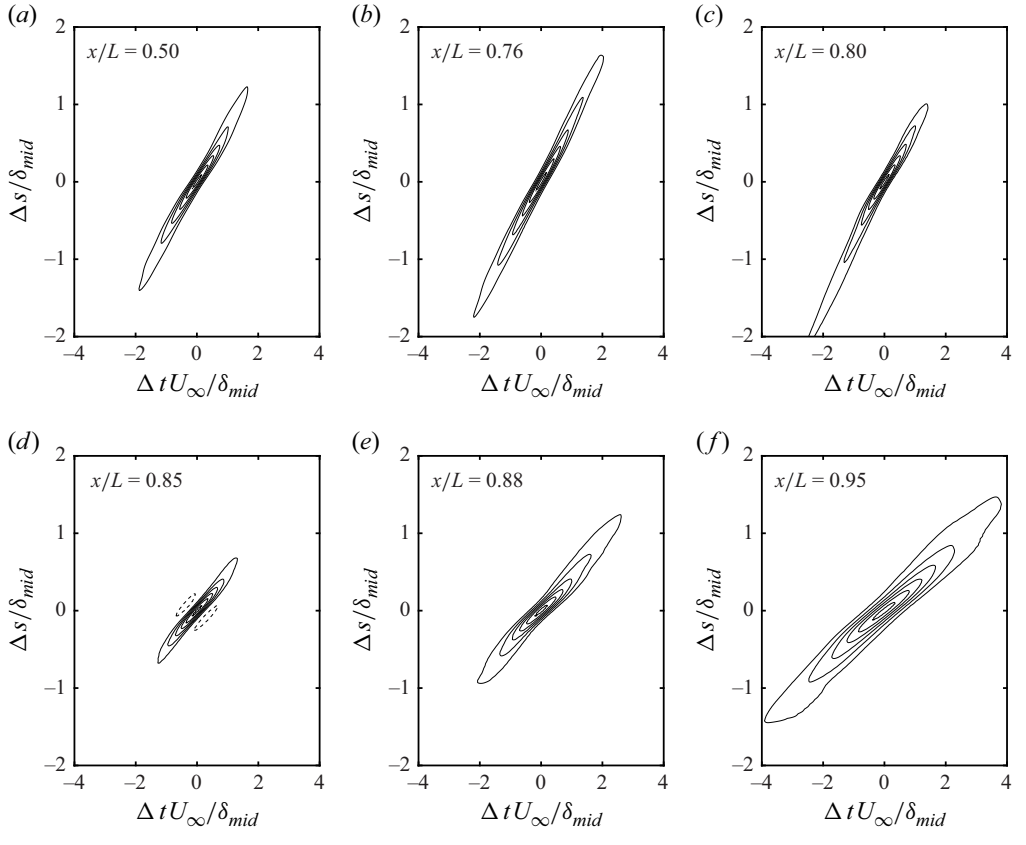

Figure 22. Contours of two-point correlation of wall pressure fluctuations as functions of streamwise spatial and temporal separations: (*a*) $x/L = 0.50$, (*b*) $x/L = 0.76$, (*c*) $x/L = 0.80$, (*d*) $x/L = 0.85$, (*e*) $x/L = 0.88$, (*f*) $x/L = 0.95$. The solid lines represent contours ranging from 0.2 to 0.95 with increments of 0.15, while the dashed line denotes the contour at -0.1.

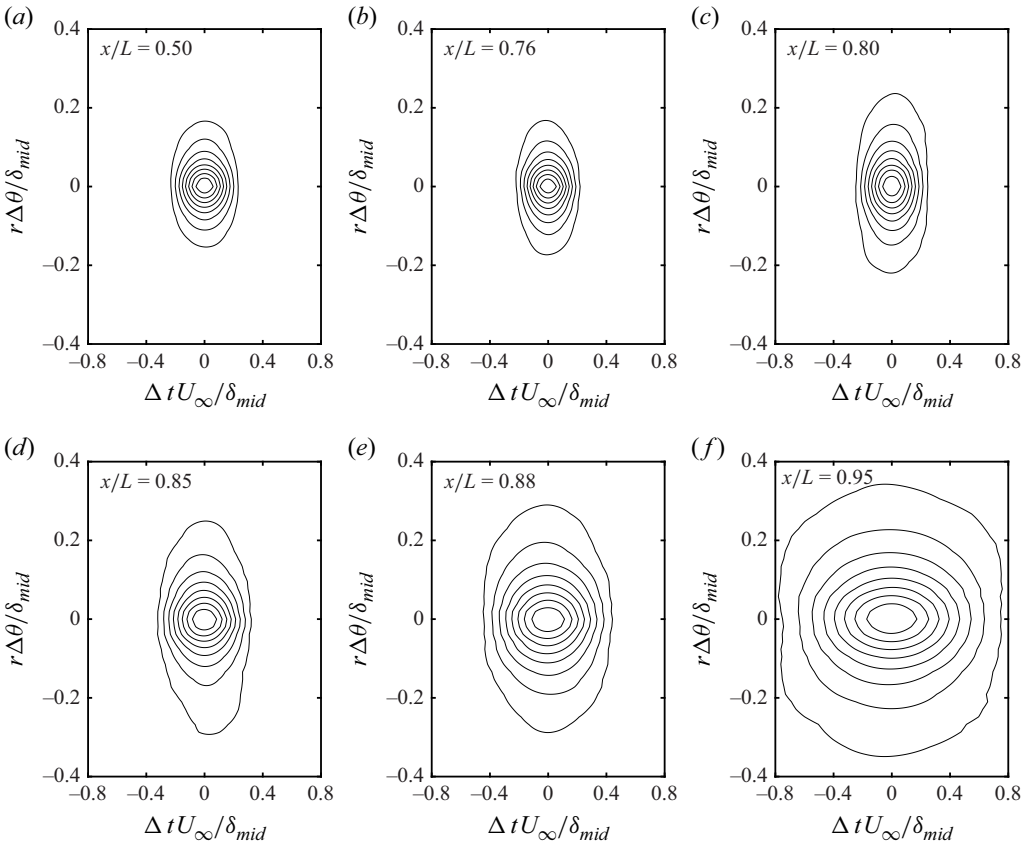

Figure 23. Contours of two-point correlation of wall pressure fluctuations as a function of transverse spatial and temporal separations: (*a*) $x/L = 0.50$, (*b*) $x/L = 0.76$, (*c*) $x/L = 0.80$, (*d*) $x/L = 0.85$, (*e*) $x/L = 0.88$, (*f*) $x/L = 0.95$. Contour levels are from 0.2 to 0.9 with increments of 0.1.

respectively. The APG markedly reduces convection velocities, while the FPG enhances them. Streamwise coherence exhibits strong sensitivity to pressure gradient magnitude. In the APG onset region (figure 22*c*), the streamwise correlation scale decreases rapidly downstream, with further reductions under strengthening APG. Conversely, FPG significantly amplifies streamwise coherence, particularly at large separations (evident in low-level contours), aligning with prior studies (Na & Moin 1998; Caiazzo *et al.* 2023). As the APG weakens (figures 22*d–f*), the streamwise correlation scale recovers, accompanied by contour broadening. This recovery reflects an increase in the correlation time scale of wall pressure fluctuations. Notably, at $x/L = 0.85$, where the APG is strongest, negative contours are observed on both sides of the convective ridge (figure 22*d*). This phenomenon will be discussed further in figure 24.

Figure 23 presents two-point correlation contours of wall pressure fluctuations as functions of transverse spatial and temporal separations. Unlike streamwise coherence, transverse coherence exhibits weaker sensitivity to pressure gradients. Under mild FPG (figure 23*b*), the contours remain nearly unchanged compared to the ZPG (figure 23*a*). However, with increasing APG (figures 23*c,d*), the transverse correlation scale grows as contours elongate spatially – a trend consistent with prior flat-plate and aerofoil studies (Na & Moin 1998; Caiazzo *et al.* 2023). Notably, as the APG diminishes downstream

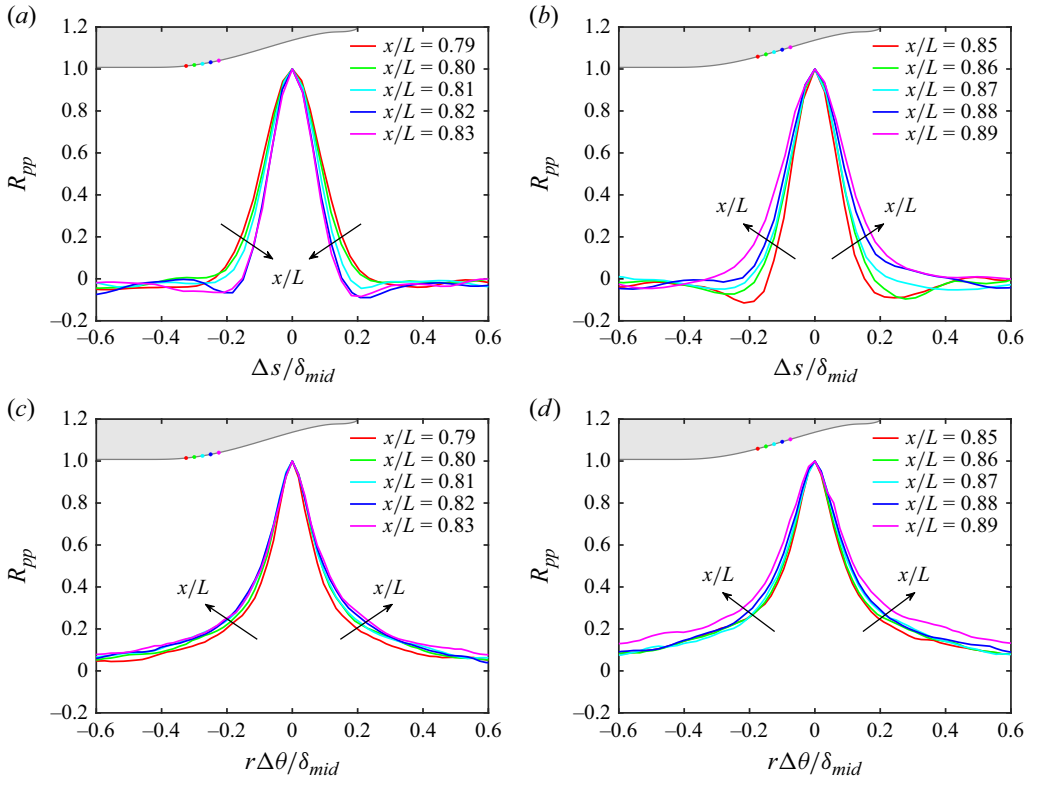

Figure 24. Two-point correlation coefficients of wall pressure fluctuations as a function of (*a*,*b*) streamwise separation and (*c*,*d*) transverse separation in regions (*a*,*c*) APG-1, (*b*,*d*) APG-2.

(figure 23*d–f*), the transverse integral scale continues to increase rather than decrease. This behaviour aligns with observations on another LES study of BOR (Zhou *et al.* 2020), but contrasts with flat-plate conclusions (Na & Moin 1998; Caiazzo *et al.* 2023), which can be attributed to the contraction of geometry at the stern. As the turbulent structures and shear layer motions shift away from the wall, larger outer-layer structures, characterised by longer correlation lengths, dominate the coherence of wall pressure fluctuations. This aligns with the simultaneous growth of streamwise and transverse correlation scales (figures 22(*d–f*) and 23(*d–f*)) and the shift of spectral energy to lower frequencies (figure 14*d,e*).

In terms of the effect of transverse curvature, APG and the contraction of the SUBOFF stern's geometry drive rapid boundary layer thickening, amplifying the curvature ratio δ/r_0 to $\sim 6:1$ at $x/L = 0.95$ (figure 10). Although transverse curvature is generally considered to have a minor effect on wall pressure fluctuations in previous studies (Willmarth & Yang 1970; Neves *et al.* 1994; Piquet & Patel 1999), its influence becomes non-negligible when δ/r_0 is relatively large. Interestingly, the observed increase in correlation scales with increasing transverse curvature at the stern contradicts the findings of Willmarth & Yang (1970) regarding transverse curvature effects. Their study concluded that transverse curvature leads to smaller streamwise and transverse integral scales, suggesting that pressure-generating motions occur closer to the wall compared to a flat plate. However, the experiments by Willmarth & Yang (1970) were conducted on a straight cylinder, with the flow approximately in a ZPG state. For the SUBOFF geometry, the flow

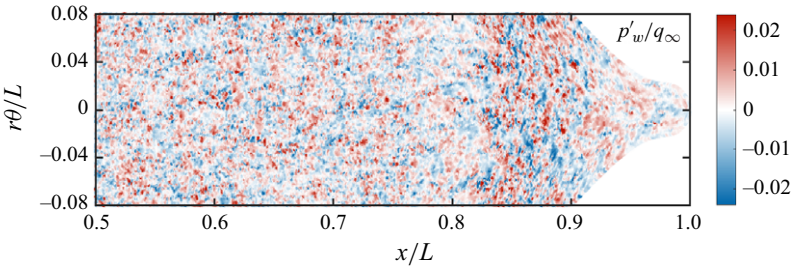

Figure 25. Instantaneous non-dimensional wall pressure fluctuation field plotted versus $r\theta$ and x.

history near the stern shows great difference due to the distinct geometric configuration. The influence of streamwise curvature variations seems to be more significant than that of transverse curvature. To isolate the influence of transverse curvature alone, additional simulation cases would be required.

Figure 24 presents two-point correlation coefficients of wall pressure fluctuations as functions of streamwise separation and transverse separation in the APG-1 and APG-2 regions. Under APG conditions, the streamwise correlation curves (figures 24*a*,*b*) exhibit distinct negative lobes flanking the central positive peak at $\Delta s/\delta_{mid} = \pm 0.2$, which is consistent with the observation in figure 22(*d*). Additionally, the streamwise integral length scales of wall pressure fluctuations are smaller than the transverse counterparts, which can also be observed in the instantaneous non-dimensional wall pressure fluctuation field. As shown in figure 25, the amplitude of wall pressure fluctuations increases rapidly within the stern APG region, accompanied by a sharp reduction in the streamwise integral scale. As the APG weakens, the streamwise integral scale gradually recovers. Beyond $x/L > 0.9$, it is evident that wall pressure fluctuations exhibit larger streamwise and transverse scales. This observation is consistent with the analysis above, primarily attributed to turbulent structure and the local maximum Reynolds shear stress shifting away from the wall. The structure of wall pressure fluctuations in this region tends to more isotropic.

5. Conclusions

In this study, wall-resolved large-eddy simulations (WRLES) of flow over an axisymmetric body of revolution (BOR) (the DARPA SUBOFF bare model) at $Re_L = 1.1 \times 10^6$ are performed within a finite-volume framework. To fully resolve near-wall small-scale vortices, we employ a computational grid exceeding 540 million cells. Extensive validation of the numerical methodology is conducted, and the results demonstrate great agreement with experimental data (Huang *et al.* 1992) and prior WRLES studies (Kumar & Mahesh 2018). In the parallel mid-body region, wall pressure fluctuations show close alignment with planar experiment (Schewe 1983), DNS (Na & Moin 1998), LES (Cohen & Gloerfelt 2018) and empirical models (Chase 1980; Goody 2004; Lee 2018). Building on this, we investigate scaling laws and space–time correlations of wall pressure fluctuations at the stern. The key findings and conclusions are as follows.

Due to the coexistence of convex and concave streamwise curvatures, the flow over the SUBOFF model in the stern region features alternating zones of favourable and adverse pressure gradients (FPGs and APGs), which exhibits greater complexity than the BOR configuration studied experimentally by Balantrapu *et al.* (2023). By synthesising streamwise curvature and pressure gradient effects, the stern flow is divided into six distinct regions. In the APG-2 region (straight contraction segment, $0.85 < x/L < 0.90$),

the r.m.s. value of wall pressure fluctuations decreases alongside the wall shear stress, maintaining a ratio $p_{w,rms}/\tau_w = 6$. This aligns with the Balantrapu *et al.* (2023) experimental observations, but yields a lower ratio than their reported $p_{w,rms}/\tau_w = 7$. The ratio $p_{w,rms}/\tau_w$ is considered to be influenced by the local Reynolds number and the pressure gradient intensity. Further investigation is required to establish a comprehensive scaling framework accounting for these effects.

The present study also finds that the constant $p_{w,rms}/\tau_w$ ratio holds only for equilibrium boundary layers under steady APG. In non-equilibrium regions with strong streamwise curvature or rapidly varying APG (APG-1 and APG-3), this relationship breaks down, and conventional inner or inner–outer variable scaling methods become largely ineffective. Neither the local dynamic pressure q_e nor the wall shear stress τ_w serves as a suitable pressure scale. Instead, scaling wall pressure fluctuations using the local maximum Reynolds shear stress $-\rho\langle u_s u_n\rangle_{max}$ achieve significantly improved collapse across the entire stern region. This underscores near-wall turbulent shear motion as the dominant contributor of wall pressure fluctuations in the non-equilibrium region, and establishes $-\rho\langle u_s u_n\rangle_{max}$ as a robust pressure scaling parameter. The magnitude and location of $-\rho\langle u_s u_n\rangle_{max}$ significantly influence the spectral levels of wall pressure fluctuations across different frequency bands. Downstream of the stern, as the turbulence intensity and $-\rho\langle u_s u_n\rangle_{max}$ shift away from the wall, the high-frequency wall pressure component decays persistently, with pre-multiplied spectra gradually shifting towards lower frequencies. For axisymmetric boundary layers with varying pressure gradient, δ, U_e and $-\rho\langle u_s u_n\rangle_{max}$ emerge as more appropriate length, velocity and pressure scales, respectively.

In terms of the space–time characteristics, as anticipated, the APG reduces the convection velocity of wall pressure fluctuations, shortens the streamwise correlation length scale, and increases the transverse correlation length scale. However, as the APG weakens (APG-2 and APG-3), the streamwise correlation length scale recovers, while the transverse correlation length scale continues to grow, which can be attributed to the contraction of SUBOFF geometry and differences in the upstream flow history compared to previously studied cases (Willmarth & Yang 1970). As $-\rho\langle u_s u_n\rangle_{max}$ weakens and shifts away from the wall, larger outer-layer structures – characterised by longer decay lengths – dominate the coherence of wall pressure fluctuations. However, the shear layer motions typically drive the wall pressure dynamics not by directly slapping the wall. They exert a strong but indirect influence by modulating the near-wall boundary layer turbulence, thereby affecting the wall pressure fluctuations. Quantifying this influence clearly requires further work. A feasible approach is to rigorously examine the source terms in the pressure Poisson equation, including the mean-shear term and the nonlinear term, and to quantify their contributions to wall pressure fluctuations across different frequency bands.

Finally, we think that this study holds significant practical value for naval and aerospace applications. Given the prohibitive computational cost of WRLES for predicting wall pressure fluctuations in high-Reynolds-number turbulent flows, our results are benchmarked against many established empirical models (Corcos 1964; Chase 1980; Witting 1986; Goody 2004; Smol'yakov 2006; Rozenberg *et al.* 2012; Hu & Herr 2016; Lee 2018). For wavenumber–frequency spectrum modelling, the Chase I model shows great agreement with the current dataset in the low-wavenumber regime, reaffirming its utility for rapid engineering predictions. However, several limitations warrant attention. For instance, the observed asymmetry in spectral energy near the convective ridge remains unaccounted for in existing models. Furthermore, wavenumber–frequency spectrum

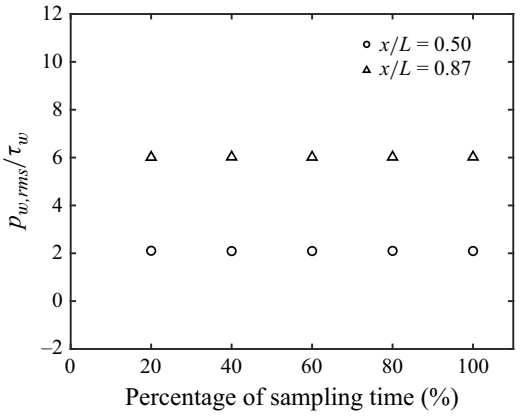

Figure 26. Stationarity test of flow statistics: wall pressure r.m.s. normalised by τ_w for each section.

models tailored for flows under APG require further development to address the unique spectral redistribution caused by APG-induced turbulence modulation.

Acknowledgements. The computations in this paper were run on the Siyuan-1 cluster supported by the Centre for High Performance Computing at Shanghai Jiao Tong University, and we express our gratitude.

Funding. This study was supported by the National Natural Science Foundation of China (51909160, 52131102) and the National Key Research and Development Programme of China (2022YFC2806705).

Declaration of interests. The authors report no conflict of interest.

Appendix A. Stationarity test with respect to the length of sampling time

To verify whether the flow is fully developed and the statistical properties remain invariant with sampling time, we conduct a stationarity test similar to that in He *et al.* (2025) in this appendix. The present simulation is run for six flow-past times, with the first 2.5 flow-past times used for flow development, and the remaining 3.5 flow-past times used for statistical analysis. The sampling data of the 3.5 flow-past times are divided into five sections, with each section increasing in length by 20 %. Figure 26 shows the wall pressure r.m.s. normalised by τ_w for each section. The results are largely unaffected by the sampling duration, indicating that the flow is fully developed and the sampling time is sufficient.

Appendix B. Detailed comparisons of scaling laws in the APG-1 and APG-3 regions

Figure 27 compares non-dimensional PSD of wall pressure fluctuations in the APG-1 region ($0.79 < x/L < 0.85$) using different scaling approaches. As shown in figure 27(*b*), inner scaling fails to collapse the high-frequency spectral components due to the decreasing τ_w, aligning with prior studies of non-equilibrium TBLs (Na & Moin 1998; Cohen & Gloerfelt 2018; Caiazzo *et al.* 2023). The Zagarola–Smits scaling successfully collapses the spectra at high frequencies, while discrepancies exceeding 10 dB remain at low frequencies. This failure of conventional inner and mixed inner–outer scaling methods reflects the flow's departure from equilibrium. Supporting this, figure 12 reveals a 134 % increase in dimensionless ratio $p_{w,rms}/q_e$ (0.0053 to 0.0124) and a 273 % rise in $p_{w,rms}/\tau_w$ (1.5 to 5.6) across this region. These diverging trends confirm that neither q_e nor τ_w provides a reliable pressure scale for APG TBL in non-equilibrium conditions. In contrast, scaling the wall pressure fluctuation spectra with the local maximum Reynolds

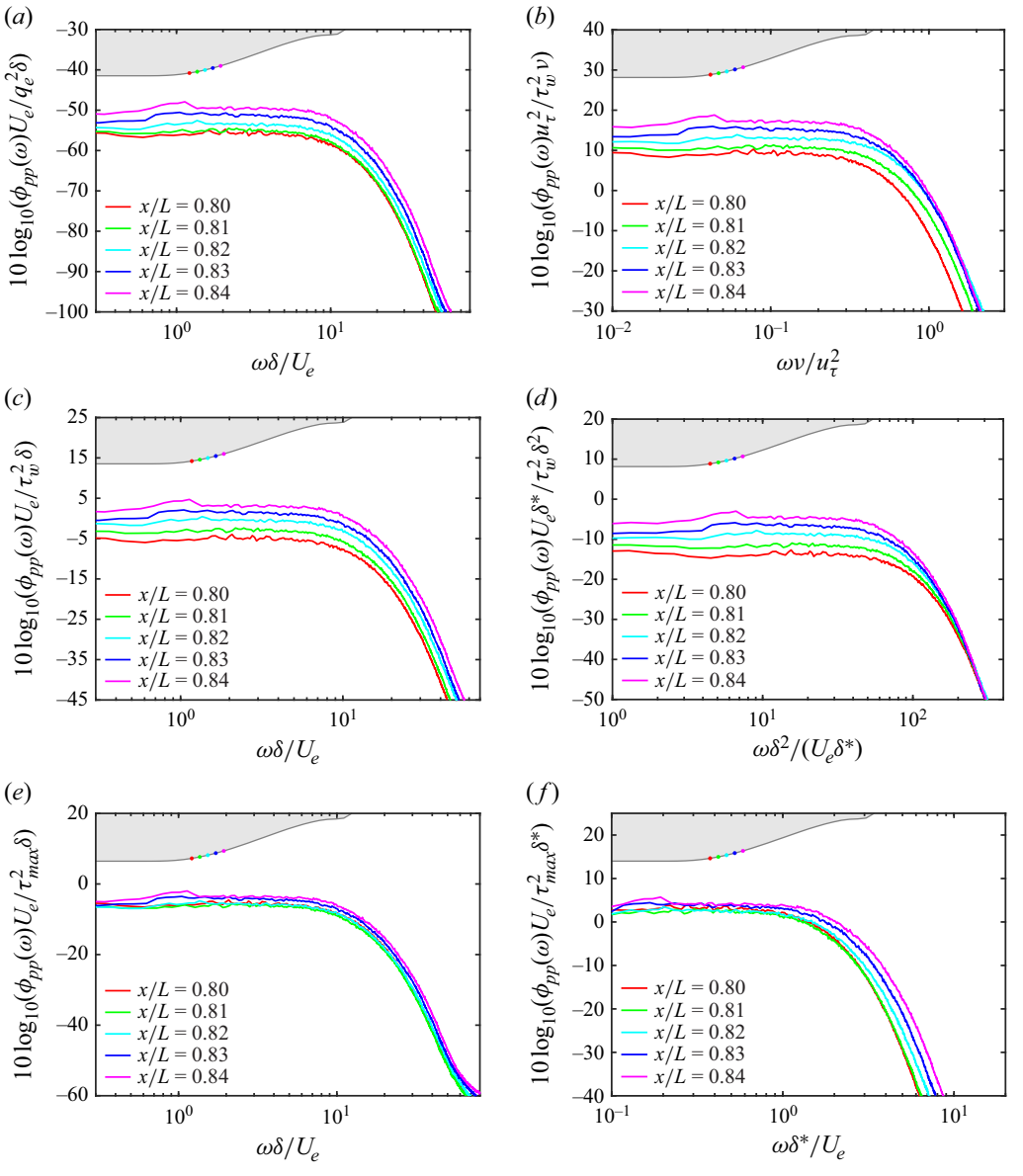

Figure 27. Non-dimensional PSD of wall pressure fluctuations under different scaling methods in the APG-1 region ($0.79 < x/L < 0.85$): (*a*) outer scaling (q_e, δ and U_e); (*b*) inner scaling (τ_w, δ_v and u_τ); (*c*) mixed scaling (τ_w, δ and U_e); (*d*) Zagarola–Smits scaling (τ_w, δ^2/δ^* and U_e); (*e*) Reynolds shear stress scaling (τ_{max}, δ and U_e); (*f*) displacement thickness scaling (τ_{max}, δ^* and U_e).

shear stress τ_{max} achieves a collapse within 3 dB across the entire frequency range. The 59 % increase of $p_{w,rms}/\tau_{max}$ (1.7 to 2.7) is much smaller than $p_{w,rms}/q_e$ and $p_{w,rms}/\tau_w$ in the APG-1 region.

Figure 28 presents non-dimensional PSD plots of wall pressure fluctuations in the APG-3 region ($0.90 < x/L < 0.94$), where the APG weakens progressively as the Clauser parameter β_e decreases from 7.2 to 0. Figure 14(*e*) shows a broadband attenuation of spectral energy across all frequencies in this region. None of the conventional scaling

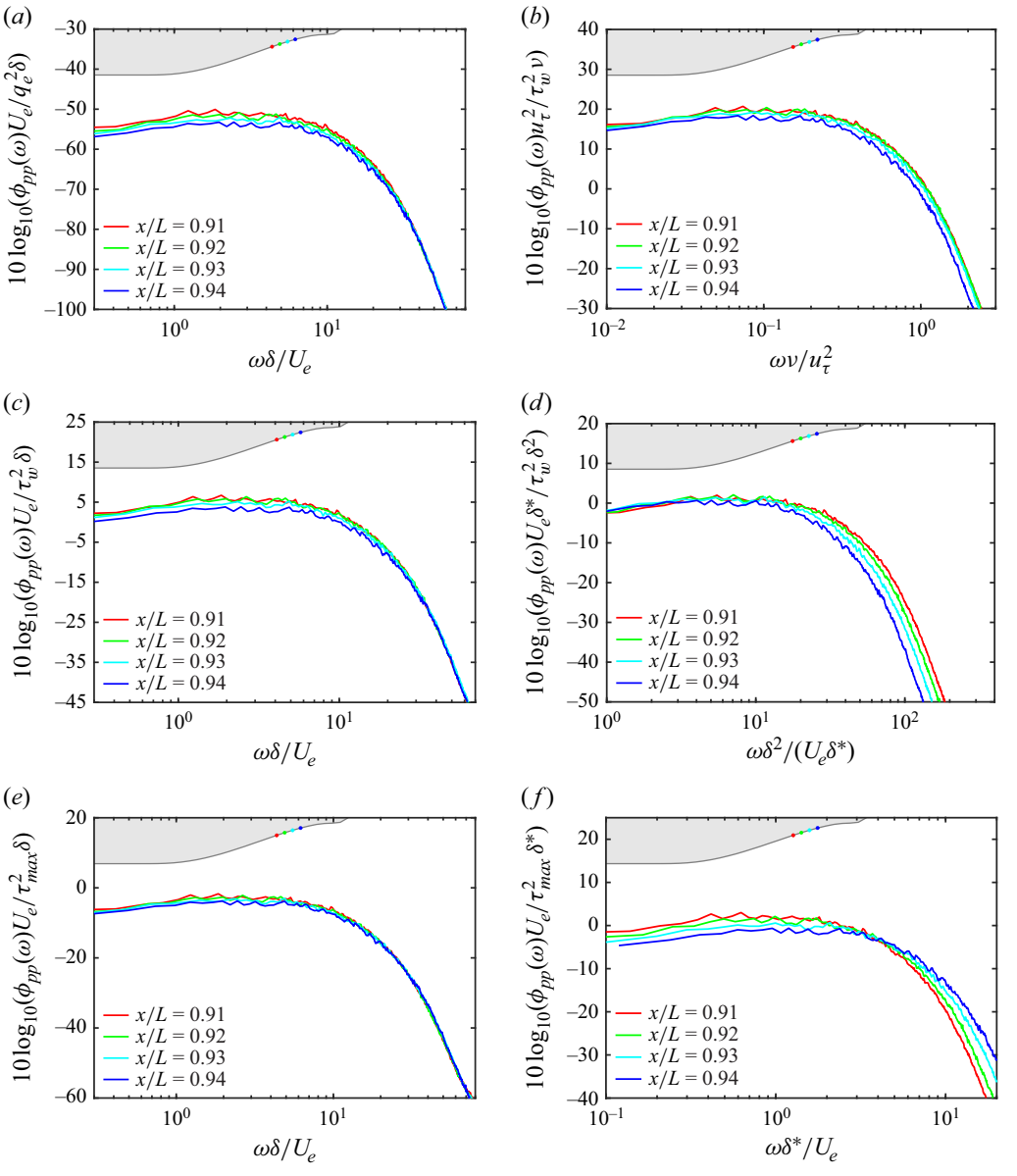

Figure 28. Non-dimensional PSD of wall pressure fluctuations under different scaling methods in the APG-3 region ($0.90 < x/L < 0.94$): (*a*) outer scaling (q_e, δ and U_e); (*b*) inner scaling (τ_w, δ_v and u_τ); (*c*) mixed scaling (τ_w, δ and U_e); (*d*) Zagarola–Smits scaling (τ_w, δ^2/δ^* and U_e); (*e*) Reynolds shear stress scaling (τ_{max}, δ and U_e); (*f*) displacement thickness scaling (τ_{max}, δ^* and U_e).

methods (figures 28*a–c*) achieves full spectral collapse in all frequency bands, which demonstrates the persistent challenge in scaling wall pressure spectra for boundary layers under transient APG conditions, irrespective of whether β_e is increasing or decreasing during the flow evolution. In comparison, the Reynolds shear stress scaling also achieves the best collapse across the entire frequency range, suggesting its robustness as a scaling parameter for axisymmetric TBL under APG conditions, irrespective of the boundary layer's equilibrium state.

Appendix C. Wavenumber–frequency spectra model of wall pressure fluctuations

In this appendix, we provided the formulas and details of wavenumber–frequency spectra model of wall pressure fluctuations used in § 4, including the Corcos model (Corcos 1964), Chase I model (Chase 1980) and Witting model (Witting 1986).

The Corcos model (Corcos 1964) is the earliest wavenumber–frequency spectrum model and remains widely used today. The model begins by fitting the temporal Fourier transform of the space–time correlation function for TBL wall pressure fluctuations. Subsequently, it applies a generalised Fourier transform in the spatial domain to derive the wavenumber–frequency spectrum model. The model expression is given as

$$\phi(k_x, k_z, \omega) = \phi(\omega)\left(\frac{\alpha_1\alpha_3}{\pi^2 k_c^2}\right)\left[\alpha_1^2 + \left(\frac{k_x}{k_c} - 1\right)^2\right]\left[\alpha_3^2 + \left(\frac{k_z}{k_c}\right)^2\right], \tag{C1}$$

where k_x and k_z are the streamwise and spanwise wavenumbers, respectively, $k_c = \omega/U_c$ represents the convective wavenumber, with U_c being the convection velocity (approximately 60–80 % of the inflow velocity U_∞), and α_1 and α_3 are empirical constants representing the decay rates of spatial correlations in the streamwise and spanwise directions. According to Bull's experiment (Bull 1967), for a smooth flat plate, $\alpha_1 = 0.1$, $\alpha_3 = 0.715$.

The Chase I model (Chase 1980) is a classic incompressible flow model based on the Poisson equation, which does not need the self-spectral model as input. It models the rapid and slow source terms of the Poisson equation separately. The model expression is given as

$$\begin{aligned}\phi(k_x, k_z, \omega) &= \phi_r(k_x, k_z, \omega) + \phi_s(k_x, k_z, \omega)\\ &= \rho^2 u_\tau^3\left(C_r k_x^2 K_r^{-5} + C_s k_x^2 K_s^{-5} + C_s k_z^2 K_s^{-5}\right),\end{aligned} \tag{C2}$$

where

$$K_i^2 = \frac{(\omega - U_c k_x)^2}{h_i^2 u_\tau^2} + k_x^2 + k_z^2 + (b_i\delta)^{-2}, \quad i = r, s, \tag{C3}$$

where the subscripts r and s denote the rapid and slow parts, respectively. The key model coefficients are set to be $C_r = 0.0745$, $C_s = 0.0474$, $b_r = 0.756$, $b_s = 0.378$, $h_r = 3$ and $h_s = 3$.

The Witting model (Witting 1986), which also targets incompressible flows, adopts a distinct modelling approach compared to other models. It postulates that the generation of fluctuating pressure in incompressible flows is closely tied to TBL phenomena, such as bursts and sweeps. Viewing these as dipole sound sources, the model constructs a stochastic theoretical framework based on these phenomena. Witting interprets each burst/sweep as an event, and the wavenumber–frequency spectrum is derived as the Fourier transform of the fluctuating pressure induced by countless such events, combined with their respective coefficients. The model expression is given as

$$\phi(k_x, k_z, \omega) = \frac{8}{3}\overline{p^2}\frac{\delta^{*3}}{U_c}\frac{A\hat{\omega}^2}{\xi^5}\int_{\xi_{min}}^{\xi_{max}} y^4\,\mathrm{e}^{-2y}\,\mathrm{d}y, \tag{C4}$$

where

$$\left.\begin{gathered}\xi = \hat{k}_{xz} + C\,|\hat{\omega} - \hat{k}_x|, \\ \xi_{max} = \frac{\xi\delta_{max}}{\delta^*}, \quad \xi_{min} = \frac{\xi\delta_{min}}{\delta^*}, \\ \hat{k}_x = k_x\delta^*, \quad \hat{k}_z = k_z\delta^*, \quad \hat{k}_{xz} = \sqrt{\hat{k}_x^2 + \hat{k}_z^2}, \\ \hat{\omega} = \frac{\omega\delta^*}{U_c}, \quad A = \frac{C}{\pi}\frac{1}{\left(1 + \dfrac{2}{3C^3}\right)\ln\left(\dfrac{\delta_{max}}{\delta_{min}}\right)}.\end{gathered}\right\} \tag{C5}$$

The mean square $\overline{p^2}$ is modelled as

$$\overline{p^2} = 0.015U_c^2u_\tau^2\rho^2. \tag{C6}$$

The key coefficients of the Witting model, C, δ_{max} and δ_{min}, are set to be $C = 8$, $\delta_{max} = 8\delta^*$ and $\delta_{min} = 0.005\delta^*$.

To obtain the two-dimensional spectra of the wall pressure fluctuations, integration is required over k_z of $\phi(x, k_z, \omega)$:

$$\phi(k_x, \omega) = \int_{-\infty}^{+\infty} \phi(k_x, k_z, \omega)\,\mathrm{d}k_z. \tag{C7}$$

For the Corcos model, the analytical solution of its two-dimensional spectrum can be obtained through integration. In contrast, for the Chase I and Witting models, numerical solutions are derived using the trapezoidal rule.

References

Abe, H. 2017 Reynolds-number dependence of wall-pressure fluctuations in a pressure-induced turbulent separation bubble. *J. Fluid Mech.* **833**, 563–598.

Abe, H., Matsuo, Y. & Kawamura, H. 2005 A DNS study of Reynolds-number dependence on pressure fluctuations in a turbulent channel flow. In *4th International Symposium on Turbulence and Shear Flow Phenomena*, pp. 189–194. Begel House Inc.

Abraham, B.M. & Keith, W.L. 1998 Direct measurements of turbulent boundary layer wall pressure wavenumber–frequency spectra. *J. Fluids Engng* **120** (1), 29–39.

Alam, M.M. 2020 A review of transverse curvature effect on friction force and leading-edge flow. *Ocean Engng* **218**, 107573.

Balantrapu, N.A., Alexander, W.N. & Devenport, W. 2023 Wall-pressure fluctuations in an axisymmetric boundary layer under strong adverse pressure gradient. *J. Fluid Mech.* **960**, A28.

Balantrapu, N.A., Fritsch, D.J., Millican, A.J., Hickling, C., Gargiulo, A., Vishwanathan, V., Alexander, W.N. & Devenport, W.J. 2020 Wall pressure fluctuations in an axisymmetric turbulent boundary layer under strong adverse pressure gradient. In *AIAA Scitech 2020 Forum*, American Institute of Aeronautics and Astronautics.

Blake, W.K. 1970 Turbulent boundary-layer wall-pressure fluctuations on smooth and rough walls. *J. Fluid Mech.* **44** (4), 637–660.

Bobke, A., Vinuesa, R., Örlü, R. & Schlatter, P. 2017 History effects and near equilibrium in adverse-pressure-gradient turbulent boundary layers. *J. Fluid Mech.* **820**, 667–692.

Bull, M.K. 1967 Wall-pressure fluctuations associated with subsonic turbulent boundary layer flow. *J. Fluid Mech.* **28** (4), 719–754.

Caiazzo, A., Pargal, S., Wu, H., Sanjosé, M., Yuan, J. & Moreau, S. 2023 On the effect of adverse pressure gradients on wall-pressure statistics in a controlled-diffusion aerofoil turbulent boundary layer. *J. Fluid Mech.* **960**, A17.

Chase, D.M. 1980 Modeling the wavevector–frequency spectrum of turbulent boundary layer wall pressure. *J. Sound Vib.* **70** (1), 29–67.

Choi, H. & Moin, P. 1990 On the space–time characteristics of wall-pressure fluctuations. *Phys. Fluids* **2** (8), 1450–1460.

CLAUSER, F.H. 1954 Turbulent boundary layers in adverse pressure gradients. *J. Aeronaut. Sci.* **21** (2), 91–108.
COHEN, E. & GLOERFELT, X. 2018 Influence of pressure gradients on wall pressure beneath a turbulent boundary layer. *J. Fluid Mech.* **838**, 715–758.
COLEMAN, G.N., RUMSEY, C.L. & SPALART, P.R. 2018 Numerical study of turbulent separation bubbles with varying pressure gradient and Reynolds number. *J. Fluid Mech.* **847**, 28–70.
CORCOS, G.M. 1964 The structure of the turbulent pressure field in boundary-layer flows. *J. Fluid Mech.* **18** (3), 353–378.
FAN, G.Q., LIU, Y., ZHAO, W.W. & WAN, D.C. 2024*a* Effect of wall stress models and subgrid-scale models for flow past a cylinder at Reynolds number 3900. *Phys. Fluids* **36** (1), 015152.
FAN, G.Q., ZHU, J., ZHAO, W.W. & WAN, D.C. 2024*b* A comparative study between wall-resolved and wall-modeled large eddy simulation of turbulent channel flows. In *34th International Ocean and Polar Engineering Conference*, pp. 220–226. OnePetro.
FARABEE, T.M. & CASARELLA, M.J. 1991 Spectral features of wall pressure fluctuations beneath turbulent boundary layers. *Phys. Fluids* **3** (10), 2410–2420.
FRANCIS, R., EBENEZER, D.D., BHATTACHARYYA, S.K. & SHARMA, R. 2023 Estimation of wavenumber–frequency spectra of wall pressure due to turbulent flow over a flat plate using large-eddy simulation. *Phys. Fluids* **35** (6), 065110.
GOODY, M. 2004 Empirical spectral model of surface pressure fluctuations. *AIAA J.* **42** (9), 1788–1794.
GRIFFIN, K.P., FU, L. & MOIN, P. 2021 General method for determining the boundary layer thickness in nonequilibrium flows. *Phys. Rev. Fluids* **6** (2), 024608.
GROVES, N.C., HUANG, T.T. & CHANG, M.S. 1989 *Geometric Characteristics of DARPA SUBOFF Models: (DTRC Model Nos. 5470 and 5471)*. David Taylor Research Center.
HARUN, Z., MONTY, J.P., MATHIS, R. & MARUSIC, I. 2013 Pressure gradient effects on the large-scale structure of turbulent boundary layers. *J. Fluid Mech.* **715**, 477–498.
HE, K.J., ZHAO, W.W. & WAN, D.C. 2025 Physical characteristics of wall pressure fluctuations for fully developed turbulent annular channel flows. *Phys. Fluids* **37** (4), 045133.
HE, K.J., ZHOU, F.C., ZHAO, W.W. & WAN, D.C. 2024*a* Wall-modeled large eddy simulation for a highly decelerated axisymmetric turbulent boundary layer. In *34th International Ocean and Polar Engineering Conference*. OnePetro.
HE, X., HUANG, Q.G., SUN, G.C. & WANG, X.H. 2022 Numerical research of the pressure fluctuation of the bow of the submarine at different velocities. *J. Mar. Sci. Engng* **10** (9), 1188.
HE, Y.H., ZHOU, F.C., ZHAO, W.W. & WAN, D.C. 2024*b* Grid resolution requirements for wall-resolved large eddy simulation of wall pressure fluctuations in turbulent channel flows. In *34th International Ocean and Polar Engineering Conference*. OnePetro.
HU, N. & HERR, M. 2016 Characteristics of wall pressure fluctuations for a flat plate turbulent boundary layer with pressure gradients. In *22nd AIAA/CEAS Aeroacoustics Conference*. American Institute of Aeronautics and Astronautics.
HUANG, T., LIU, H.L., GROVES, N.C., FORLINI, T., BLANTON, J. & GOWING, S. 1992 Measurements of flows over an axisymmetric body with various appendages in a wind tunnel: the DARPA SUBOFF experimental program. In *Proceedings of the 19th Symposium on Naval Hydrodynamics*. National Academy Press.
ISSA, R.I. 1986 Solution of the implicitly discretised fluid flow equations by operator-splitting. *J. Comput. Phys.* **62** (1), 40–65.
JIANG, P., LIAO, S.J. & XIE, B. 2024 Large-eddy simulation of flow noise from turbulent flows past an axisymmetric hull using high-order schemes. *Ocean Engng* **312**, 119150.
JIMÉNEZ, J., HOYAS, S., SIMENS, M.P. & MIZUNO, Y. 2010*a* Turbulent boundary layers and channels at moderate Reynolds numbers. *J. Fluid Mech.* **657**, 335–360.
JIMÉNEZ, J.M., HULTMARK, M. & SMITS, A.J. 2010*b* The intermediate wake of a body of revolution at high Reynolds numbers. *J. Fluid Mech.* **659**, 516–539.
JIMÉNEZ, J.M., REYNOLDS, R.T. & SMITS, A.J. 2010*c* The effects of fins on the intermediate wake of a submarine model. *J. Fluids Engng* **132**, 031102.
KEITH, W.L., HURDIS, D.A. & ABRAHAM, B.M. 1992 A comparison of turbulent boundary layer wall-pressure spectra. *J. Fluids Engng* **114** (3), 338–347.
KIM, J. 1989 On the structure of pressure fluctuations in simulated turbulent channel flow. *J. Fluid Mech.* **205**, 421–451.
KITSIOS, V., SEKIMOTO, A., ATKINSON, C., SILLERO, J.A., BORRELL, G., GUNGOR, A.G., JIMÉNEZ, J. & SORIA, J. 2017 Direct numerical simulation of a self-similar adverse pressure gradient turbulent boundary layer at the verge of separation. *J. Fluid Mech.* **829**, 392–419.

KLINE, S.J., REYNOLDS, W.C., SCHRAUB, F.A. & RUNSTADLER, P.W. 1967 The structure of turbulent boundary layers. *J. Fluid Mech.* **30** (4), 741–773.

KRAICHNAN, R.H. 1964 Kolmogorov's hypotheses and Eulerian turbulence theory. *Phys. Fluids* **7** (11), 1723–1734.

KUMAR, P. & MAHESH, K. 2018 Large-eddy simulation of flow over an axisymmetric body of revolution. *J. Fluid Mech.* **853**, 537–563.

LEE, M. & MOSER, R.D. 2015 Direct numerical simulation of turbulent channel flow up to $Re_\tau \approx 5200$. *J. Fluid Mech.* **774**, 395–415.

LEE, S. 2018 Empirical wall-pressure spectral modeling for zero and adverse pressure gradient flows. *AIAA J.* **56** (5), 1818–1829.

LIU, C.Q., GAO, Y., TIAN, S.L. & DONG, X.R. 2018 Rortex – a new vortex vector definition and vorticity tensor and vector decompositions. *Phys. Fluids* **30** (3), 035103.

LIU, Y., WANG, H.P., WANG, S.Z. & HE, G.W. 2023 A cache-efficient reordering method for unstructured meshes with applications to wall-resolved large-eddy simulations. *J. Comput. Phys.* **480**, 112009.

MARUSIC, I., MCKEON, B.J., MONKEWITZ, P.A., NAGIB, H.M., SMITS, A.J. & SREENIVASAN, K.R. 2010 Wall-bounded turbulent flows at high Reynolds numbers: recent advances and key issues. *Phys. Fluids* **22** (6), 065103.

MONTY, J.P., HUTCHINS, N., NG, H.C.H., MARUSIC, I. & CHONG, M.S. 2009 A comparison of turbulent pipe, channel and boundary layer flows. *J. Fluid Mech.* **632**, 431–442.

MORSE, N. & MAHESH, K. 2021 Large-eddy simulation and streamline coordinate analysis of flow over an axisymmetric hull. *J. Fluid Mech.* **926**, A18.

MORSE, N. & MAHESH, K. 2023 Tripping effects on model-scale studies of flow over the DARPA SUBOFF. *J. Fluid Mech.* **975**, A3.

NA, Y. & MOIN, P. 1998 The structure of wall-pressure fluctuations in turbulent boundary layers with adverse pressure gradient and separation. *J. Fluid Mech.* **377**, 347–373.

NEVES, J.C. & MOIN, P. 1994 Effects of convex transverse curvature on wall-bounded turbulence. Part 2. The pressure fluctuations. *J. Fluid Mech.* **272**, 383–406.

NEVES, J.C., PARVIZ, M. & MOSER, R.D. 1994 Effects of convex transverse curvature on wall-bounded turbulence. Part 1. The velocity and vorticity. *J. Fluid Mech.* **272**, 349–382.

NICOUD, F. & DUCROS, F. 1999 Subgrid-scale stress modelling based on the square of the velocity gradient tensor. *Flow Turbul. Combust.* **62** (3), 183–200.

PANTON, R.L., LEE, M. & MOSER, R.D. 2017 Correlation of pressure fluctuations in turbulent wall layers. *Phys. Rev. Fluids* **2** (9), 094604.

PATEL, V.C., NAKAYAMA, A. & DAMIAN, R. 1974 Measurements in the thick axisymmetric turbulent boundary layer near the tail of a body of revolution. *J. Fluid Mech.* **63** (2), 345–367.

PIQUET, J. & PATEL, V.C. 1999 Transverse curvature effects in turbulent boundary layer. *Prog. Aerosp. Sci.* **35** (7), 661–672.

POSA, A. & BALARAS, E. 2016 A numerical investigation of the wake of an axisymmetric body with appendages. *J. Fluid Mech.* **792**, 470–498.

POSA, A. & BALARAS, E. 2020 A numerical investigation about the effects of Reynolds number on the flow around an appended axisymmetric body of revolution. *J. Fluid Mech.* **884**, A41.

ROZENBERG, Y., ROBERT, G. & MOREAU, S. 2012 Wall-pressure spectral model including the adverse pressure gradient effects. *AIAA J.* **50** (10), 2168–2179.

SCHATZMAN, D.M. & THOMAS, F.O. 2017 An experimental investigation of an unsteady adverse pressure gradient turbulent boundary layer: embedded shear layer scaling. *J. Fluid Mech.* **815**, 592–642.

SCHEWE, G. 1983 On the structure and resolution of wall-pressure fluctuations associated with turbulent boundary-layer flow. *J. Fluid Mech.* **134**, 311–328.

SCHLOEMER, H.H. 1966 Effects of pressure gradients on turbulent boundary-layer wall-pressure fluctuations. *J. Acoust. Soc. Am.* **40** (5_Suppl), 1254.

SILLERO, J.A., JIMÉNEZ, J. & MOSER, R.D. 2013 One-point statistics for turbulent wall-bounded flows at Reynolds numbers up to $\delta^+ \approx 2000$. *Phys. Fluids* **25** (10), 105102.

SIMPSON, R.L., GHODBANE, M. & MCGRATH, B.E. 1987 Surface pressure fluctuations in a separating turbulent boundary layer. *J. Fluid Mech.* **177**, 167–186.

SMOL'YAKOV, A.V. 2006 A new model for the cross spectrum and wavenumber–frequency spectrum of turbulent pressure fluctuations in a boundary layer. *Acoust. Phys.* **52** (3), 331–337.

SNARSKI, S.R. & LUEPTOW, R.M. 1995 Wall pressure and coherent structures in a turbulent boundary layer on a cylinder in axial flow. *J. Fluid Mech.* **286**, 137–171.

SPALART, P.R. & WATMUFF, J.H. 1993 Experimental and numerical study of a turbulent boundary layer with pressure gradients. *J. Fluid Mech.* **249**, 337–371.

TANARRO, Á., VINUESA, R. & SCHLATTER, P. 2020 Effect of adverse pressure gradients on turbulent wing boundary layers. *J. Fluid Mech.* **883**, A8.

TAYLOR, G.I. 1938 The spectrum of turbulence. *Proc. R. Soc. Lond. A* **164** (919), 476–490.

TENNEKES, H. 1975 Eulerian and Lagrangian time microscales in isotropic turbulence. *J. Fluid Mech.* **67** (3), 561–567.

VIAZZO, S., DEJOAN, A. & SCHIESTEL, R. 2001 Spectral features of the wall-pressure fluctuations in turbulent wall flows with and without perturbations using LES. *Intl J. Heat Fluid Flow* **22** (1), 39–52.

VOLINO, R.J. 2020 Non-equilibrium development in turbulent boundary layers with changing pressure gradients. *J. Fluid Mech.* **897**, A2.

WILLMARTH, W.W., WINKEL, R.E., SHARMA, L.K. & BOGAR, T.J. 1976 Axially symmetric turbulent boundary layers on cylinders: mean velocity profiles and wall pressure fluctuations. *J. Fluid Mech.* **76** (1), 35–64.

WILLMARTH, W.W. & YANG, C.S. 1970 Wall-pressure fluctuations beneath turbulent boundary layers on a flat plate and a cylinder. *J. Fluid Mech.* **41** (1), 47–80.

WILLS, J.A.B. 1971 Measurements of the wave-number/phase velocity spectrum of wall pressure beneath a turbulent boundary layer. *J. Fluid Mech.* **45** (1), 65–90.

WITTING, J.M. 1986 A spectral model of pressure fluctuations at a rigid wall bounding an incompressible fluid based on turbulent structures in the boundary layer. *Noise Control Engng J.* **26** (1), 28–43.

YANG, B.W. & YANG, Z.X. 2022 On the wavenumber–frequency spectrum of the wall pressure fluctuations in turbulent channel flow. *J. Fluid Mech.* **937**, A39.

ZHOU, D., WANG, K. & WANG, M. 2020 Large-eddy simulation of an axisymmetric boundary layer on a body of revolution. In *AIAA Aviation 2020 Forum*. American Institute of Aeronautics and Astronautics.

ZHOU, Z.T., XU, Z.Y., WANG, S.Z. & HE, G.W. 2022 Wall-modeled large-eddy simulation of noise generated by turbulence around an appended axisymmetric body of revolution. *J. Hydrodyn.* **34** (4), 533–554.